Design and Additive Manufacturing of Carbon-Fiber Reinforced Polymer Microlattice with High Stiffness and High Damping

Ruthvik Dinesh Kadam

Thesis submitted to the faculty of the Virginia Polytechnic Institute and State University in partial fulfillment of the requirements for the degree of

Master of Science
In
Mechanical Engineering

Xiaoyu (Rayne) Zheng, Chair
Robert L. West
Christopher B. Williams

September 5, 2019
Blacksburg, VA

Keywords: Multi-material additive manufacturing, carbon-fiber composites, viscoelastic materials, cellular structures, high damping

Design and Additive Manufacturing of Carbon-Fiber Reinforced Polymer Microlattice with High Stiffness and High Damping

Ruthvik Dinesh Kadam

ABSTRACT

Carbon fiber reinforced polymer (CFRP) composites are known for their high stiffness-to-weight and high strength-to-weight ratios and hence are of great interest in several engineering fields such as aerospace, automotive and defense. However, despite their light weight, high stiffness and high strength, their application in these fields is limited due to their poor energy dissipation and vibration damping capabilities. This thesis presents a two-phase microlattice design to overcome this problem. To realize this design, a novel tape casting integrated multi-material stereolithography system is developed and mechanical properties of samples fabricated using this system are evaluated. The design incorporating a stiff phase (CFRP) and a high loss phase, exhibiting high stiffness as well as high damping, is studied via analytical and experimental approaches. To investigate its damping performance, mechanical properties at small-strain and large-strain regimes are measured through dynamic material analysis (DMA) and quasi-static cyclic compression tests respectively. It is seen that both intrinsic (small-strain) and structural (large-strain) damping in terms of a figure of merit (FOM), $E^{1/3}\tan\delta/\rho$, can be enhanced by a small addition of a high loss phase in Reuss configuration. Moreover, it is seen that structural damping is improved at low relative densities due to the presence of elastic buckling during deformation. For design usefulness, tunability maps, displaying FOM in terms of design parameters, are developed by curve fitting of experimental measurements. The microlattice design is also evaluated quantitatively by comparing it with existing families of materials in a stiffness-loss map, which shows that the design is as stiff as commercial CFRP composites and as dissipative as elastomers.

Design and Additive Manufacturing of Carbon-Fiber Reinforced Polymer Microlattice with High Stiffness and High Damping

Ruthvik Dinesh Kadam

GENERAL AUDIENCE ABSTRACT

Carbon fiber reinforced polymer (CFRP) composites are known for their lightweight, high stiffness and high strength and hence are of great interest in several engineering fields such as aerospace, automotive and defense. However, despite these advantages, their application in these fields is limited due to their poor energy dissipation and vibration damping capabilities. This thesis presents a novel cellular lattice design to overcome this problem. Recent growth in stereolithography (SLA) has enabled the fabrication of complex structures with high resolution. Using this capability of SLA additive manufacturing, a cellular design is developed to improve both the stiffness and damping performance of CFRP composites while reducing weight. Experiments are conducted to determine the stiffness and damping properties and small and large deformations. It is seen that the stiffness and damping properties can be increased through a two-material hybrid design, comprising of a high stiffness phase and a high damping phase, arranged in a specific pattern. The microlattice design is evaluated quantitatively by comparing it with the existing families of materials using an Ashby chart. The design shows a two order-of-magnitude increase in the stiffness-damping performance when compared to commercially available CFRP.

ACKNOWLEDGMENTS

I would like to extend my most sincere appreciation to my advisor Dr. Xiaoyu (Rayne) Zheng for his mentoring and support through the course of my study. His methods and suggestions have been a motivation and inspiration and have helped me get the most out of myself. I would like to thank Zhenpeng Xu, Dr. Chan Soo Ha, and my colleagues from Oak Ridge National Laboratory, John Lindahl and Dr. Pum Kim for their continued support and inputs through the project. Without their efforts, this would not have been possible. I would also like to thank my other lab colleagues for their help and guidance. I would also like to thank committee members Dr. Robert L. West and Christopher B. Williams for taking the time to review my work.

Finally, I would like to thank all of my family and friends. They, despite the physical distance, have always encouraged and supported my work and have helped me achieve my goals.

TABLE OF CONTENTS

List of Figures vii
List of Tables ix
Chapter 1: Introduction 1
1.1. Background 1
1.2. Literature review 2
1.3. Thesis organization 7

Chapter 2: Additive manufacturing of CFRP composites 9
2.1. Introduction 9
2.2. Manufacturing process 9
2.3. Materials 10
2.4. Challenges to AM of CFRP composites 12
2.5. Post-processing and fabricated samples 16

Chapter 3: Mechanical properties of CFRP composites 18
3.1. Introduction 18
3.2. Materials 19
3.3. Methods 21
3.4. Results 23
3.4.1. Modulus tests 23
3.4.2. Dynamic tests 25
3.5. Conclusion 26
3.6. Discussion 26

Chapter 4: Analysis of viscoelastic composites. 28
4.1. Introduction 28
4.2. Figure of merit 28
4.3. Damping mechanisms 30
4.3.1. Intrinsic material damping 31

Chapter 5: Design of lightweight, high stiffness and high damping microlattice. 39
5.1. Introduction 39
5.2. Damping mechanisms in cellular structures 39
5.3. FE analysis of octet truss 40
5.4. Design for maximizing FOM 41
5.5. Investigation of damping performance of microlattice 43
5.5.1. Intrinsic damping 43
5.5.2. Structural damping 48
5.6. Quantitative assessment of CFRP microlattice design 55

Chapter 6: Applications, Conclusions and Future work 57
6.1. Applications 57
6.2. Conclusions 58
6.3. Future work 59
6.4. Research contributions 60

References 61

LIST OF FIGURES

Figure 1.1. Schematic showing the possibilities of hybrid materials [1]. The materials can be combined in different ways to achieve the desired combination of properties. 1
Figure 1.2. Stress and strain sinusoids with a phase difference. 4
Figure 1.3. Stiffness – loss map (E – tan δ) plot for common families of materials. 5
Figure 1.4. Cellular structures showing constant specific stiffness at ultralow densities [2] 7

Figure 2.1. Schematic of the projection microstereolithography technique. 10
Figure 2.2. Schematic of the UV curable CFRP resin preparation process and optical image of the resin. 11
Figure 2.3. Plot showing the increase in resin viscosity with increase in carbon fiber loading. At 20% volume fraction, the viscosity approached close to that of honey (10 Pa-s) 13
Figure 2.4. Schematic of the tape-casting integrated multi-material system to fabricate complex CFRP structures. 14
Figure 2.5. Optical images of coated CFRP resin films with different fiber loadings. . . 15
Figure 2.6. Effect of CFRP resin on curing time. (a) Cure depth of different fiber loadings with 5s cure time. (b) The variation of cure depth with an increase in exposure for 20% fiber loading resin. 16
Figure 2.7. CFRP samples printed using the described system. (a) Complex spiral ball with 10% CF loading. (b) Complex closed cell polyhedron with 5% CF loading. (c) Menger sponge with 20% CF laoding. (d) Octet truss unit cell comprising of 10% CFRP and high loss phase. 17

Figure 3.1. The distribution of fiber lengths after ball milling. 20
Figure 3.2. DMA test setup to determine the mechanical loss coefficient (tan δ) of the sample. 22
Figure 3.3. Experimental results from the tensile test. 24
Figure 3.4. Experimental results from the compressive test. 24
Figure 3.5. Experimental results from the shear test. 25
Figure 3.6. Experimental results for the mechanical loss coefficient from DMA tests. . 26
Figure 3.7. Comparison of the tensile modulus test results with theoretical bounds. . . . 27

Figure 4.1. Schematic representation of the various two-phase composites studied. 32
Figure 4.2. Stiffness-loss map for CFRP composites in various configurations obtained from theoretical predictions. It is seen that small addition of soft phase in Reuss configuration maximizes E - tan δ. 35

Figure 4.3. Variation of the FOM with the increase in the volume fraction of soft phase for Reuss and Voigt configurations. 37
Figure 4.4. Plot comparing the theoretical and experimental values of V_{soft} to maximize the FOM. 38

Figure 5.1. FE analysis of octet truss unit cell showing the stress distribution. 41
Figure 5.2. Multi-material architecture. (a) Design of lightweight, stiff, high damping microlattice with two-phase materials incorporating CFRP and soft phase. (b) Fabricated lightweight cellular CFRP microlattice having $\bar{\rho}$ = 7% with V_{soft} = 9%. (c) SEM image showing the interface between the two phases. 42
Figure 5.3. Intrinsic damping properties of a lightweight cellular CFRP microlattice having a relative density of 7 % with different volume fractions of soft phase. (a) The effective modulus (E) as a function of the soft phase ratio V_{soft}. (b) Loss tangent (tan δ) as a function of V_{soft}. 46
Figure 5.4. The intrinsic damping figure of merit as a function of V_{soft}. 47
Figure 5.5. Tunability maps for intrinsic damping performance in terms of the figure of merit obtained from experimental measurements. 48
Figure 5.6. Schematic showing the procedure to obtain tan δ from the cyclic compression test. 49
Figure 5.7. Hysteresis loops from multicyclic compression tests for 30 cycles and evolution of the loss coefficient with cycle number (inset). (a) Sample with $\bar{\rho}$ = 4% having V_{soft} = 20%. (b) Sample with $\bar{\rho}$ = 12% having V_{soft} = 20%. 50
Figure 5.8. Normalized stress-strain hysteresis loops of samples having V_{soft} = 20% with various $\bar{\rho}$. Elastic buckling behavior was observed for $\bar{\rho}$ = 4% and diminished with an increase of $\bar{\rho}$ resulting in a reduction in area of the loop. 51
Figure 5.9. Stiffness and damping results from cyclic tests. (a) The effective modulus (E) as a function of V_{soft}. The modulus was inversely proportional to an increase in V_{soft}. (b) Loss tangent (tan δ) as a function of V_{soft}. An increase in V_{soft} led to an improvement in loss tangent. 53
Figure 5.10. The figure of merit as a function of V_{soft}. FOM can be tuned to have a peak when V_{soft} is approximately 10%. 54
Figure 5.11. Tunability maps for structural damping performance in terms of the figure of merit obtained from experimental measurements. 55
Figure 5.12. Assessment of the lightweight cellular CFRP microlattice developed in this work. The orange ellipse represents the envelope of experimental results for an overall damping property. 56

Figure 6.1. Snapshot of large-scale CFRP sample printed. 59

LIST OF TABLES

Table 3.1: Formulation of the UV curable CFRP with different fiber loadings. 20

Table 5.1: Storage modulus (i.e. stiffness) and intrinsic tan δ of the samples with relative density of 7 % at small-strains. 46
Table 5.2: The coefficients of fitting equations of storage modulus (i.e. stiffness) and tan δ of the samples with relative density of 7 % at small-strains. 46
Table 5.3: Modulus [MPa] of samples. 53
Table 5.4: tan δ of samples. 53
Table 5.5: The coefficients of fitting equations of modulus of samples. 53
Table 5.6: The coefficients of fitting equations of tan δ of samples. 54

Chapter 1. Introduction

1.1 Background

For several decades, humans have performed cross-breeding among plants and animals in order to obtain a product of higher quality. Different breeds of dogs are cross-bred in order to obtain desired traits or looks. Cattles are crossbred to produce higher quality and quantity of milk. Of late, most corn grown in the United States is hybrid and this has resulted in a multi-fold increase in yield. All in all, the use of hybrid combinations to achieve properties that otherwise would be impossible to achieve has been in practice for a long time now.

Recent advances in material science have led to the application of similar principles to materials. As seen in Fig. 1.1 [1], combining two materials opens up a lot of possibilities to achieve new and improved material properties. This, as a result, has led to the development of a large number of hybrid materials such as composites, sandwich structures and cellular structures., wherein two or more materials are combined in different ways to obtain specific properties, not offered by either material alone. Traditional materials occupy specific regions on the Ashby chart. By tuning the topological distribution of materials, geometry of the structure, volume fractions of the constituent materials, new regions in the Ashby chart can be accessed [3]. This gives us a wider choice for material selection for different applications.

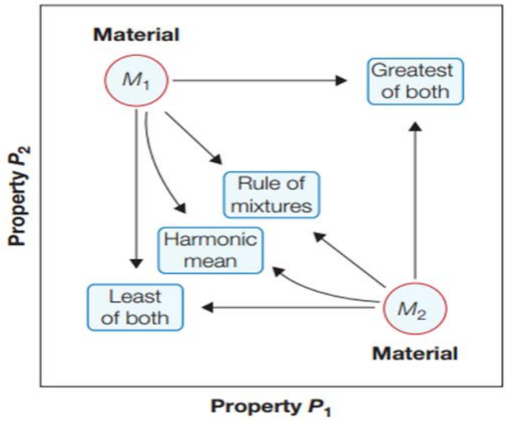

Figure 1.1. Schematic showing the possibilities of hybrid materials [1]. The materials can be combined in different ways to achieve the desired combination of properties.

Carbon fiber reinforced polymer (CFRP) is one such revolutionary composite hybrid material. It consists of carbon fibers usually arranged in a thermoset resin such as epoxy. CFRP composites are known for their high stiffness-to-weight, high strength-to-weight ratios, corrosion resistance among other properties. As a result, they have found widescale applications in the aerospace, automotive, civil, shipbuilding, sporting industries along with an ever-increasing number of applications in other fields. However, CFRP composites have one major drawback. They suffer from poor energy dissipation and damping capability because failure occurs with very little or no plastic deformation due to their brittle nature. As a result, its application in structural applications where vibration damping is required is limited.

In this thesis, a method to overcome this disadvantage of CFRP through the use of hybrid materials is demonstrated. Multi-material additive manufacturing is used to strategically distribute materials in a microlattice structure in order to increase the damping capabilities of CFRP while having minimal effect on the stiffness.

1.2. Literature review

Mechanical vibration, in a basic sense, can be defined as a phenomenon in which an object oscillates about an equilibrium point. Mechanical vibrations, in most cases, are undesirable, leading to energy loss, as in the case of engines and motors, and noise as in the case of tires, aerospace panels. For years, designers have worked on minimizing vibration in components to increase its service life and efficiency. As a result, vibration damping becomes an important consideration in the design of a successful component. Vibration damping can be defined as the control of unwanted oscillations in a component. In mechanical systems, vibration damping is classified into two types: passive damping and active damping [4]. Active damping employs external control systems to damp vibrations. This study, however, focusses on passive damping mechanisms, which occurs as a result of the properties inherent to the system. Viscoelastic materials, viscous fluids, shape memory alloys. are some examples of passive damping materials. The damping properties of materials can be represented in several different ways. The most commonly used representations of damping capacity include the loss tangent (tan δ), loss factor

(η), specific damping capacity (ψ), inverse quality factor (Q^{-1}) and damping ratio (ζ) [4]. The damping representation of importance in this study is the loss tangent, also known as mechanical loss coefficient or tan delta (tan δ). The loss tangent (tan δ) is representative of the damping capability of a material. Higher values of tan δ indicate higher damping capability.

For a viscoelastic material under dynamic loading, the stress and strain sinusoids are out of phase. The phase angle is denoted as δ. The loss tangent is defined as the tangent of the angle of phase lag between the stress and strain sinusoids (Fig. 1.2) [5]. Sinusoids with a phase difference are commonly represented as complex exponential notations [6]. As a result, the modulus of viscoelastic materials in complex form is denoted as –

$E^* = E' + iE''$	(1.1)

Where, E^* is the complex modulus, E' is the storage modulus and E'' is the loss modulus. The storage modulus represents the component of stress-strain ratio in phase with the applied strain and the loss modulus represents the component that is 90° out of phase. The magnitude of the complex modulus is denoted as $E^* = \sqrt{E'^2 + E''^2}$ and the tangent of the phase lag (δ) is-.

$\tan\delta = \frac{E''}{E'}$	(1.2)

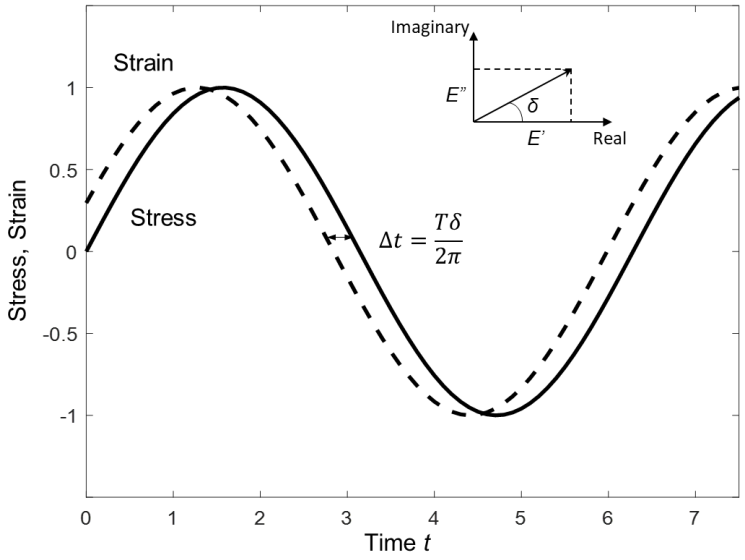

Figure 1.2. Stress and strain sinusoids with a phase difference [5].

Traditional materials such as metals, alloys and ceramics have high stiffness. However, the stress and strain sinusoids in these materials are almost in phase with each other and thus have very low values of tan δ. As a result, they provide poor damping. On the other hand, materials such as elastomers have large phase differences between their stress and strain sinusoids and thereby exhibit large tan δ values. They provide high damping but are, however, compliant and not suitable for structural applications. CFRP composites are known for their high stiffness and light weight. However, like other stiff materials, CFRP composites exhibit near elastic behavior and suffer from poor damping, thereby limiting their application for the purpose of energy dissipation. It is hard to find a traditional material that has both high damping and high stiffness. Figure 1.3. shows the Ashby chart for Young's modulus vs. tan δ for common families as materials. As seen, most materials lie on the line with a slope of -1, indicating that they all follow a similar trend, i.e. high stiffness usually is accompanied by low damping and vice versa. This trend calls for the study of hybrid materials approach of combining two materials to achieve both high stiffness and high damping simultaneously.

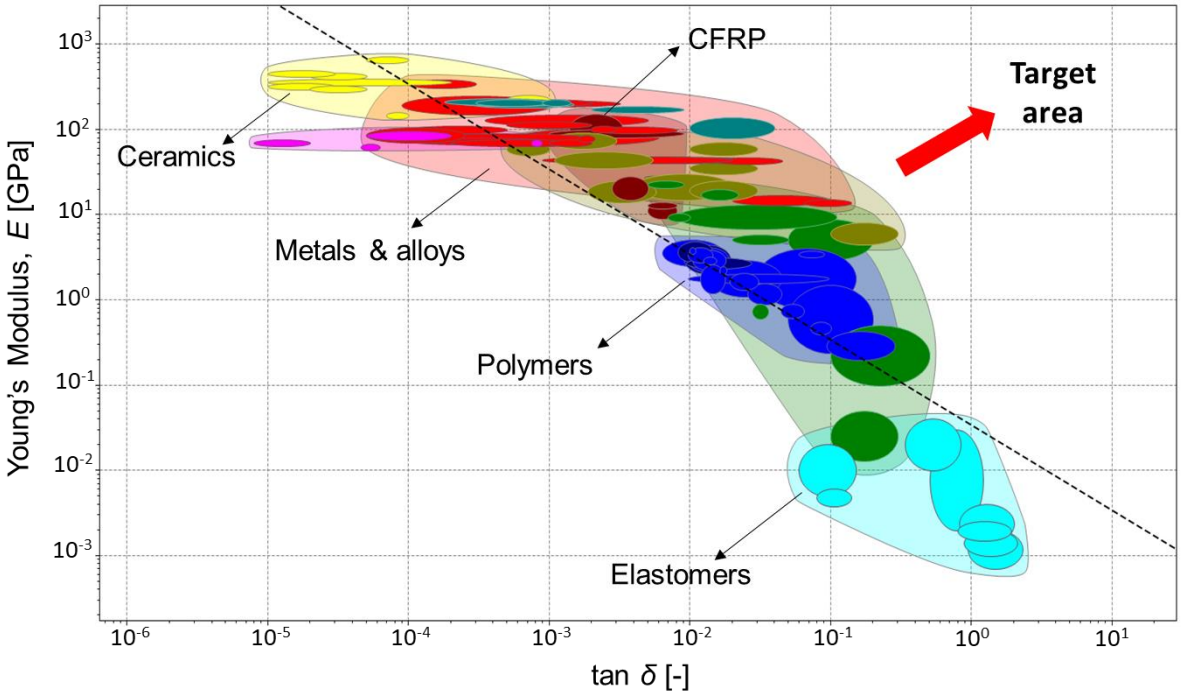

Figure 1.3. Stiffness – loss map (E – tan δ) plot for common families of materials.

In order to fabricate hybrid materials, the possibilities provided by additive manufacturing (AM) is explored. Additive manufacturing (AM), also referred to as 3D printing or rapid prototyping or direct digital manufacturing, is a manufacturing process in which material is added at desired locations instead of removed as in the case of traditional manufacturing processes. In recent times, there has been a rapid escalation in the popularity of AM processes due to its benefits over traditional manufacturing. AM allows us to manufacture complex designs, giving the designer more freedom, resulting in more efficient parts. For example, solid structures can be replaced by lattice structures to reduce the weight of a part. AM allows for mass customization. Each part can be designed as per the customer's needs. Due to this advantage of AM, it is being widely used in the jewelry and dental industry. AM also allows for tailorable properties. Due to the flexibility in the structure design and material choice provided by AM, a new area of research focusing on the use of AM to realize multi-functional materials is on the rise.

Based on the material and machine technology used, the American Society for Testing and Materials (ASTM) group "ASTM F42 – Additive Manufacturing" classified AM processes into 7 categories, namely – vat photopolymerization, material jetting, binder jetting, material extrusion,

powder bed fusion, sheet lamination and direct energy deposition. The process of concern in this study is vat photopolymerization. It makes use of a vat filled with a photo-curing resin. A 1D point or 2D image is projected onto the resin, resulting in a layer by layer construction of the desired model.

Stereolithography (SLA) is once such vat photopolymerization technique that allows for the fabrication of complex geometries with high resolution. This process is also known for its smooth surface finish and strong layer adhesion. Due to these advantages, it proves to be a promising choice to design hybrid materials with tailorable properties. CFRP composites fabricated by FFF have been well studied [7] [8] [9]. However, this method cannot be used because it is not possible to fabricate high resolution multi-material specimens. To overcome this drawback, SLA fabrication methodology was considered. However, the fabrication of CFRP composites using SLA is challenging and needs to be studied before it can be used in this work.

Due to the high resolution of SLA, it has been widely used in the fabrication of cellular materials [10] [11] [12]. Recently, cellular materials have been studied extensively due to their unique mechanical, thermal and electrical properties [13] [14]. It has been seen that these materials can exhibit unique properties such as high stiffness and strength [15] [16] [17] [18], impact protection [19] [20] [21] and piezoelectricity [22] and are of significant interest in various engineering fields. Zheng et al. reported a class of cellular material that provide near-constant specific stiffness even at ultra-low densities (Fig. 1.4) [2]. The desired properties of cellular structures can be achieved by using a periodic architecture of unit cells. The properties of periodic cellular structures are determined by their geometry (i.e., topology) and the constituent materials. Applications incorporating the periodic cellular structures particularly in vibration damping have been also previously studied [23] [24]. Moreover, studies have shown increases in the damping performance of the cellular materials through dissipative elements [25] and negative stiffness inclusions [26] [27].

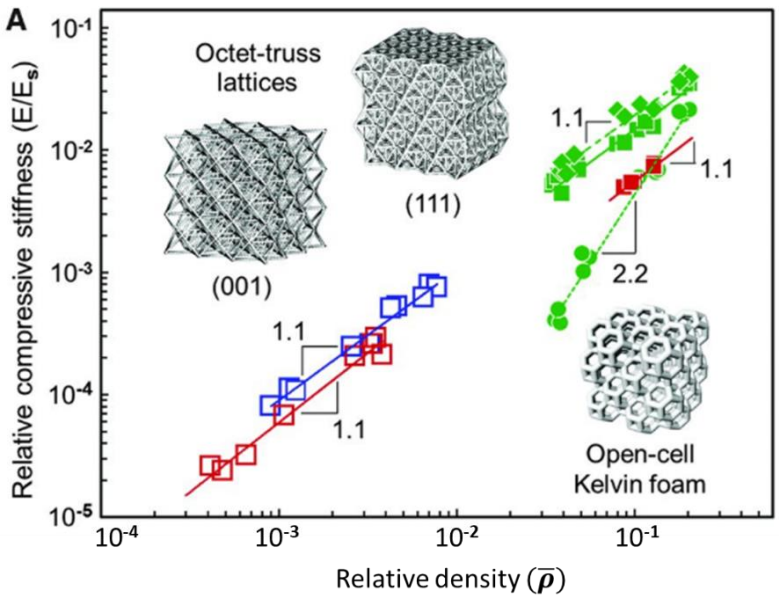

Figure 1.4. Cellular structures showing constant specific stiffness at ultralow densities [2].

In this work, an AM methodology utilizing multi-material projection micro-stereolithography (PμSL) to fabricate mesoscale CFRP composites is developed. The mechanical properties of the printed composites are tested. Using this manufacturing technique and leveraging the benefits of hybrid cellular structures, a microlattice design to increase the stiffness - damping pair while reducing the weight of CFRP composites is presented and studied. The performance of the design is quantified in terms of the figure of merit (FOM), $E^{1/3}\tan\delta/\rho$, where E is the Young's modulus, $\tan\delta$ is the mechanical loss coefficient and ρ is the relative density of the cellular structure. Experimental measurements of the stiffness and damping at small and large strains are obtained. For design usefulness, tunability maps describing the controllability of the microlattice in terms of FOM is presented. The microlattice is then evaluated by comparing with commercially available CFRP composites and also other families of materials.

1.3. Thesis organization

Chapter 2 describes the multi-material stereolithography technique. The various challenges to the 3D printing of multi-material CFRP composites are addressed. This process is then used to fabricate high-resolution CFRP cellular structures with soft phase embedded in them. Chapter 3 studies the mechanical properties of CFRP composites fabricated using the system. Materials and

testing methods are described in detail and the test results are compared with theoretical bounds. Chapter 4 presents the analysis of several two-phase viscoelastic composites to increase the stiffness-loss pair for bulk CFRP composites. The viscoelastic composite along with volume fractions of stiff and soft phases required to maximize the stiffness-loss is determined. Chapter 5 presents the cellular structure for maximizing the FOM. Results from chapter 4 are used to design the cellular structure. The variation of FOM with respect to volume fraction of soft phase and relative density of cellular structure is shown through tunability maps. An Ashby chart comparing the results with other families of materials is presented. Lastly, chapter 6 presents applications of the design and proposes ideas for future work.

Chapter 2: Additive manufacturing of CFRP composites

2.1. Introduction

CFRP composites are traditionally manufactured using techniques such as molding or vacuum bagging. These methods do not give us the benefits as seen with AM. As a result, several studies on the additive manufacturing of CFRP composites have been carried out. Out of all the AM categories, the manufacture of CFRP using fused deposition modeling (FFF) has been studied extensively due to its ease of manufacturing [7] [8] [9]. However, this method cannot be used because it is not possible to fabricate high resolution multi-material specimens. To overcome this drawback, SLA fabrication methodology was considered. However, the manufacture of CFRP composites using SLA is challenging and has not been studied extensively. In this chapter, a projection micro-stereolithography (PμSL) technique for the fabrication of CFRP composites is demonstrated.

2.2. Manufacturing process

Fabrication of high-resolution parts using projection micro-stereolithography techniques has been previously studied [28] [10]. In this technique, a CAD model of the desired part is sliced into different groups of closely spaced images. These two-dimensional slices are subsequently digitized and sent to a DMD chip which projects the image at 405 nm wavelength through a series of lenses onto the corresponding photosensitive resin. This process initiates polymerization of the resin, converting it into solid single layer part which has the same shape of the projected image. Each cured layer is followed by a recoating process in which the stage is raised, allowing the resin to settle for the next layer. The stage is then lowered to position it for the next layer and the corresponding slice image is projected. The projected pattern is arranged corresponding to the material distribution required. A schematic of this process is shown in Fig. 2.1

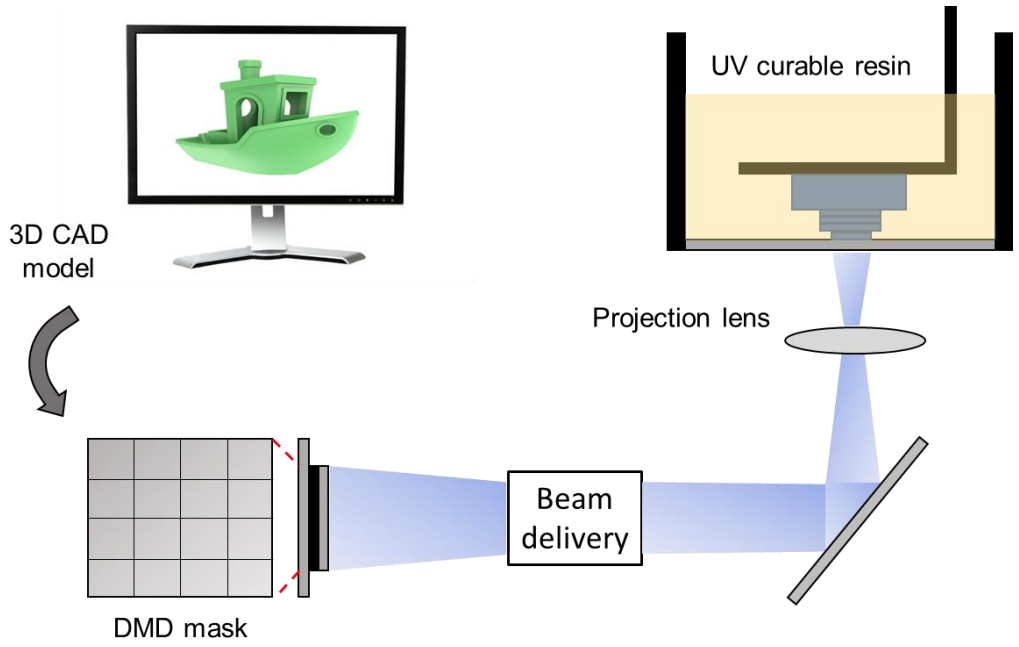

Figure 2.1. Schematic of the projection microstereolithography technique.

However, this process cannot be directly used to fabricate CFRP composites as the fibers present in the composite pose several challenges that need to be overcome. Also, this study requires the fabrication of multi-material structures. As a result, this process was revised to enable the manufacture of two-phase CFRP composites. The materials and process are defined in the coming sections.

2.3. Materials

To fabricate CFRP structures using SLA, a UV curable CFRP composite resin was developed. The composite resin consists of a UV curable matrix material reinforced with short carbon fibers. Commercially available photopolymer, Rigid, developed by Formlabs Inc., was used as the matrix. It is made up of methacrylate monomers and oligomers. This specific matrix was chosen because it had high stiffness and also showed best compatibility with the added carbon fibers among the several matrix resins that were tested. The compatibility of the fiber-matrix mixture was tested by mixing the two together and manually coating a layer and observing the coated layer quality.

The short carbon fibers with an average length of 100 microns and an average diameter of 7 microns were obtained from E&L Enterprises, Inc (product code: PC100). A photo-initiator, phenylbis (2,4,6-trimethylbenzoyl) phosphine oxide (photo-initiator, PI, from Sigma-Aldrich), was added to the fiber-matrix mixture to initiate photopolymerization. A high energy ball mill was used to mix the monomer, photo-initiator and carbon fiber together. A schematic of the UV curable resin formulation is shown in Fig. 2.2.

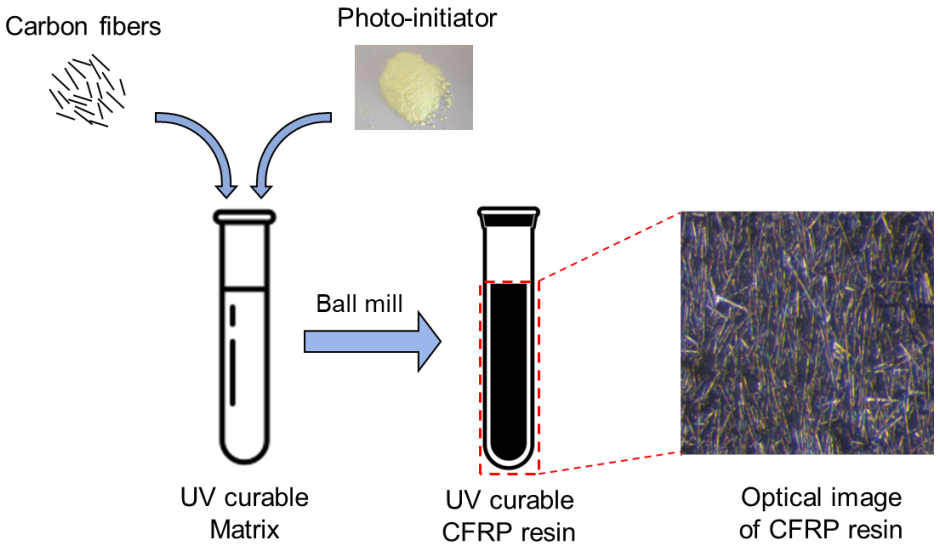

Figure 2.2. Schematic of the UV curable CFRP resin preparation process and optical image of the resin.

The volume fraction of the CFRP resin is altered by changing the ratio of matrix to carbon fibers. CFRP resin with fiber loadings of 5%, 10% and 20% were prepared. A fiber loading of 5% indicates that there is 5% of carbon fibers by volume in the UV curable matrix.

Since this study is concerned with the design of multi-material hybrid structures with high stiffness and high damping, a material with high damping (tan δ) was also considered. The material of choice was commercially available UV curable resin, Flexible resin, from Formlabs Inc. The Flexible resin is a mixture of acrylate oligomers, acrylate monomers and photo-initiators.

2.4. Challenges to AM of CFRP composites

There are three main challenges to the printing of CFRP composites. Firstly, the system needs to allow the fabrication of multiple materials. To enable this, a multiple vat system was used. A motor is setup on the x-axis of the system to move the vats depending on the material. There is also a washer tank added to the system. This cleans off the material when there is a transition from one vat to another. This entire process is automated using LabVIEW and Arduino scripts.

The second challenge to printing is the high viscosity of CFRP resins. During the printing process, resins with low viscosity can be recoated within a short time. As the viscosity increases, the resin cannot uniformly settle and recoat for the successive layer within a reasonable time when the stage is raised. With the addition of carbon fibers to the matrix, there is an increase in viscosity of the resin, making resins with high volume fractions difficult to fabricate. To determine this increase in viscosity of CFRP resin with the increase in volume fraction, a shear viscosity test was performed on the TA instruments Discovery HR-2 Hybrid Rheometer and the viscosity at zero shear was determined. The zero-shear viscosity at different volume fractions of carbon fiber is shown in Fig. 2.3. There is an exponential increase in the viscosity of the CFRP resin as the fiber loading increases. The viscosity approaches close to that of honey at 20% fiber loading CFRP. This makes it hard to fabricate resins with high fiber loadings as they do not recoat when the stage is raised and lowered for the successive layer.

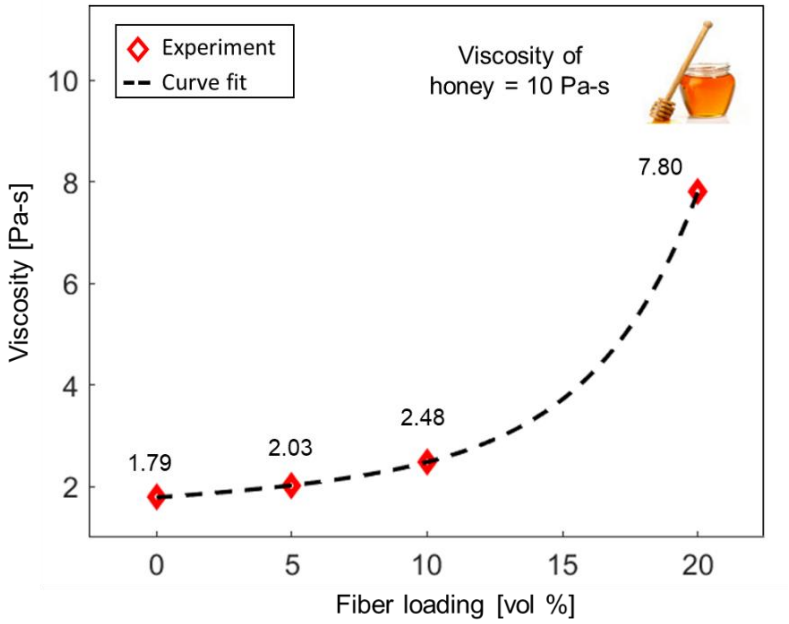

Figure 2.3. Plot showing the increase in resin viscosity with increase in carbon fiber loading. At 20% volume fraction, the viscosity approached close to that of honey (10 Pa-s).

To ensure the viscous resins can be efficiently recoated, a recoating fixture, inspired by the tape-casting technique [29], as shown in Fig. 2.4., was developed. The CAD model for this system was designed by my colleague, Zhenpeng Xu. In this method, a small amount of CFRP is extruded onto the membrane after the stage is lifted. Then a doctor blade is employed to scrape a thin CFRP film onto the membrane to ensure effective recoating for the next layer. Moreover, this technique, as reported by Song et al. [29] helps align the fibers, which is essential in achieving superior mechanical properties.

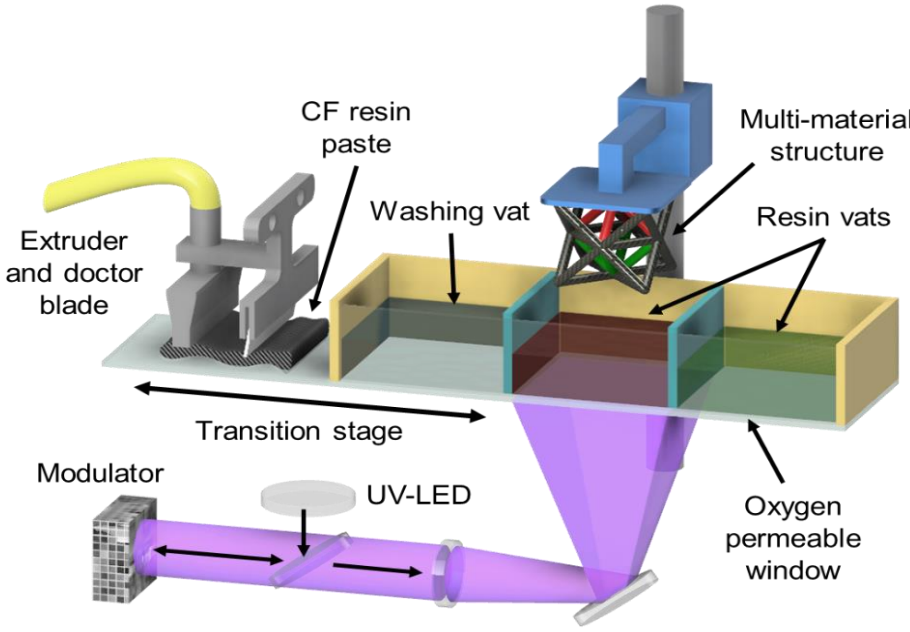

Figure 2.4. Schematic of the tape-casting integrated multi-material system to fabricate complex CFRP structures.

Even after integrating tape casting, at higher volume fractions, the problem with recoating still persists. Controlling the blade position, i.e., the distance between blade and membrane, δ_{blade}, is key to ensure the spread resin's height is high enough and that it can spread over the entire printing area. In general, the thickness of the coated layer $\delta_{coating}$ is half of the δ_{blade}. Moreover, to guarantee each layer was fully cured, $\delta_{coating}$ was set as $\delta_{coating} > k\delta$ ($k > 1$), where δ is the layer thickness and k is the safety factor [29]. The recoating quality of different fiber loading resins is tested, as shown in Fig. 2.5. It is found that at low fiber loading, the recoated layer is smooth and uniform, and the visual quality decreases as the loading increases. The maximum fiber loading that can yield a uniform layer with good quality was around 20 vol%.

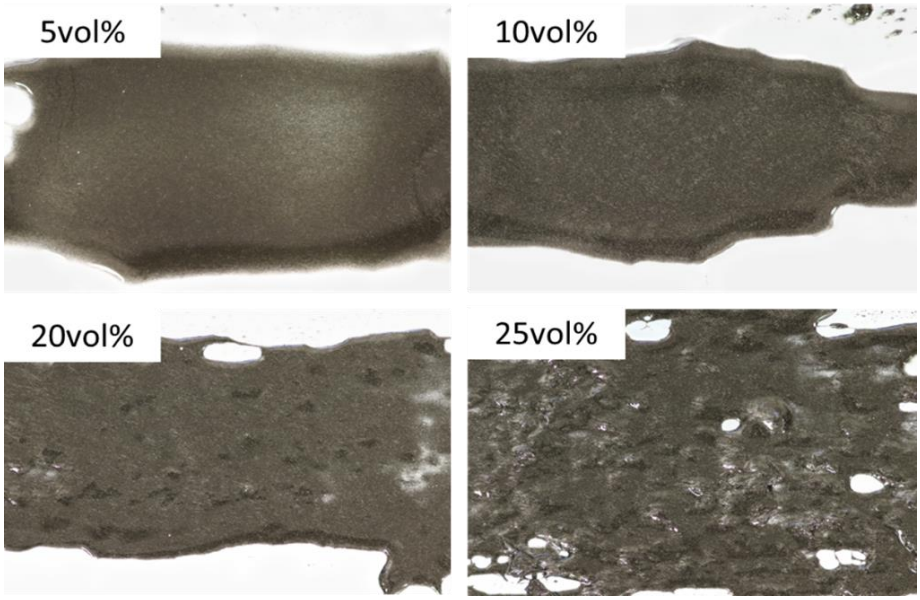

Figure 2.5. Optical images of coated CFRP resin films with different fiber loadings.

In addition to the recoating process, another challenge in the printing process is the reduced cure depth of the CFRP resin. When UV light travels through the resin, carbon fibers present in it inhibit the photocuring process by absorbing and scattering the light, thereby lowering the cure depth. Fibers also cause uneven curing of the resin due to their random distribution. This problem gets worse as the fiber loading increases. As a result, the cure depth for different fiber loadings was studied. The curing depth is related to Beer-Lambert law, which is formulated as: $Z_{cd}=1/\alpha*ln(E/E_c)$ where α is the resin absorption coefficient, E and E_c are actual and critical exposure respectively [30]. E is controlled by UV light intensity and exposure or cure time. Fig. 2.6 (a) shows the optical images of a single printed layer with different fiber loading resins with 5s cure time. It is evident that with the increase of fiber loading, the curing depth decreases. As an example, the penetration curve for the resin with 20 vol% fiber loading is plotted in Fig. 2.6 (b). The light intensity of the projection system used is 1.1W. By varying exposure time from 5s to 20s, different curing depths are obtained. For the given light intensity, the curing depth reaches to 96μm when the time goes up to 15s and saturates after that. As a result, an exposure time of 15s is used to print 20 vol% fiber loading resin. Additionally, the results indicate that the curing depth is linearly proportional to the natural logarithm of UV exposure time, which is in good agreement with the analytical model. From the curve fit, the penetration depth, D_p, is found to by 0.0087μm and the critical exposure,

E_c, is 2189.6 mJ/cm2. To ensure good adhesion between adjacent layers, the layer thickness is set at half of the curing depth in each case.

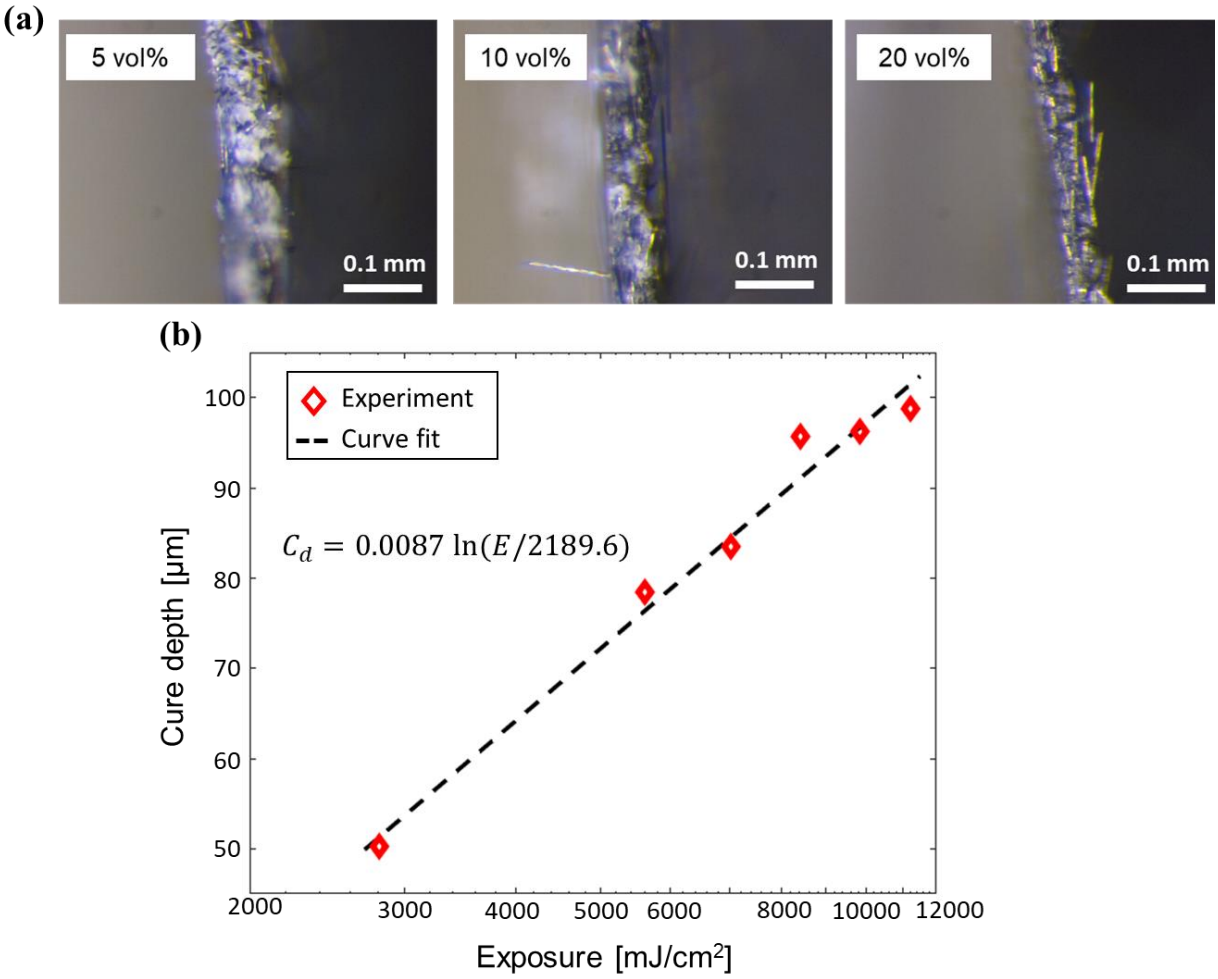

Figure 2.6. Effect of CFRP resin on curing time. (a) Cure depth of different fiber loadings with 5s cure time. (b) The variation of cure depth with an increase in exposure for 20% fiber loading resin.

2.5. Post-processing and fabricated samples

The AM technique described was designed to achieve the minimum printable 3D feature size of ~50μm in the projection (X-Y) plane. This is determined by the pixel resolution of the DMD array and the optical components. However, due to the presence of fibers, there is scattering of light, thereby slightly increasing the feature size in the XY plane. This was not studied in detail as it did

not affect the quality of the printed design. The resolution in the vertical direction (Z-direction) is determined by the driving motor, which was 5μm. As mentioned earlier, to ensure tight adhesion between neighboring layers, the layer thickness is set less than half of the cure depth i.e. 40μm. After printing, all samples were cleaned with ethanol and post-cured using ultraviolet light for 30 minutes. This process was followed by thermal post-cure at 150°F for 24 hours to ensure effective part curing. To demonstrate capabilities of the technique, a number of complex 3D samples from micro-scales to macro-scales, as shown in Fig 2.7(a)-(d), were printed. Using this system, multi-material samples with complex geometries and low size scales could be printed.

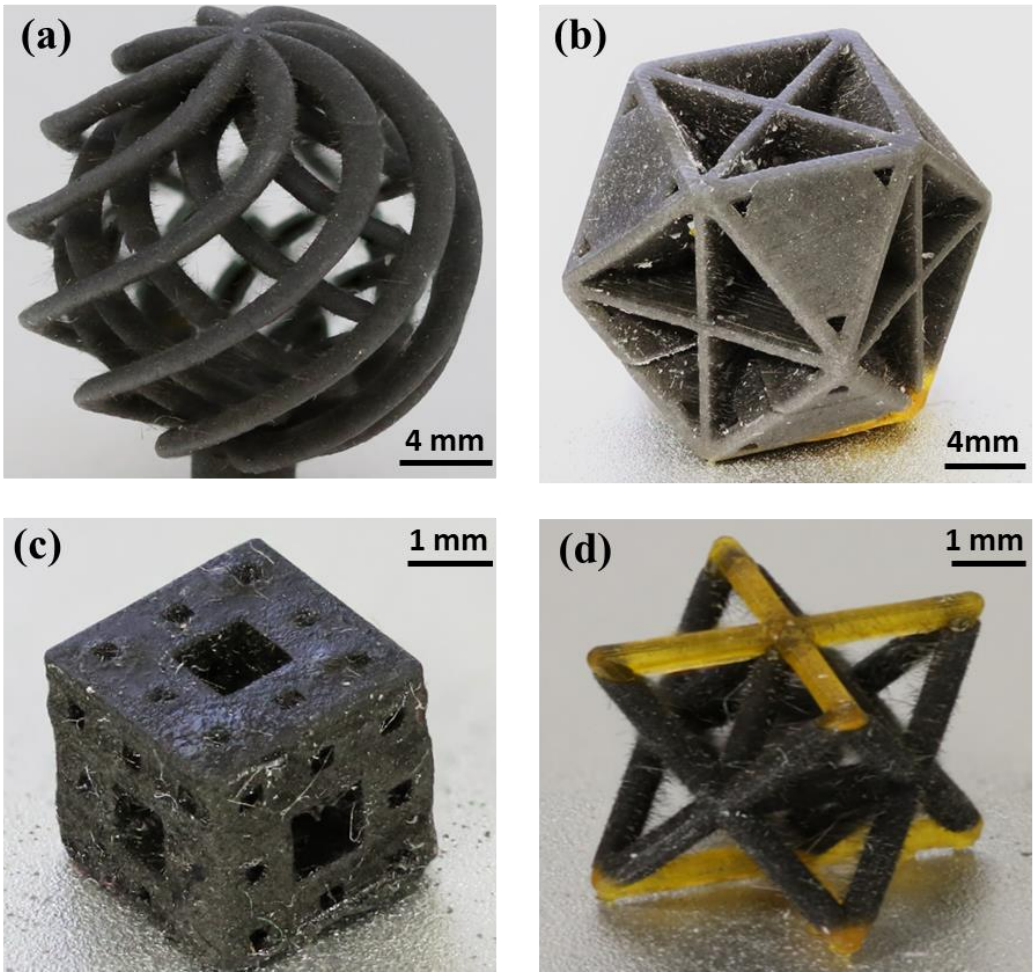

Figure 2.7. CFRP samples printed using the described system. (a) Complex spiral ball with 10% CF loading. (b) Complex closed cell polyhedron with 5% CF loading. (c) Menger sponge with 20% CF laoding. (d) Octet truss unit cell comprising of 10% CFRP and high loss phase.

Chapter 3. Mechanical Properties of CFRP composites

3.1. Introduction

Mechanical properties of the material are of great importance in the material selection process. Properties of homogeneous isotropic materials are relatively straight-forward to test and predict. However, this is not the case with composites due to their heterogeneous and anisotropic nature. The properties of heterogeneous materials like fiber-reinforced composites depends on several factors like the size of the fiber, its orientation and properties of the matrix. In addition, additive manufacturing of these composites leads to further anisotropy due to change in properties depending on the direction of the print. As a result, it becomes necessary to test these 3D printed composites.

Carbon fibers are known for their high stiffness-to-weight and high strength to weight ratio. The addition of these fibers as reinforcement in thermoset or thermoplastic polymers leads to large improvements in the stiffness and strength of the composite and thus CFRP composites have been widely used in several fields. However, the concept of SLA 3D printing of CFRP composites is fairly new and has not been well documented. As a result, it is of importance to understand the improvement in mechanical properties of CFRP composites 3D printed using SLA technology. These results can be compared to the well-defined theoretical Reuss and Voigt bounds defined as [1]:

$$E_{Voigt} = fE_r + (1-f)E_{matrix} \quad (3.1)$$

$$E_{lower} = \frac{E_r\, E_{matrix}}{fE_{matrix} + (1-f)E_r} \quad (3.2)$$

Where E_{matrix} is the modulus of the matrix, E_r is the modulus of the fiber reinforcement and f is the volume fraction of reinforcement in the composite.

This chapter summarizes the mechanical properties of SLA printed CFRP composites with different volume fractions of carbon fiber loading. The testing methods used to determine the properties of the composites printed using the system described in chapter 2 are described. The results obtained are compared with other additive manufacturing technologies and also with the theoretical bounds of the properties. Methods to reach the upper bounds are discussed. The mechanical properties of concern are the compressive Young's modulus, tensile Young's modulus, Shear modulus and the mechanical loss coefficient (tan δ) of the composite. The results from these tests are used in the design of the high stiffness and damping microlattice described in chapter 4.

3.2. Materials

The short carbon fibers with product code PC 100 were obtained from E&L Enterprises, Inc. The fibers were unsized with a carbon content of 92-94%. The average diameter of the fiber was 7 microns and the fiber length range was 80-100 microns. The density of the fibers was 1790 kg/m^3 and the Young's modulus was 206 GPa. Again, the UV curable matrix used was the commercially available Rigid photopolymer resin developed by Formlabs, Inc. A photo-initiator, phenylbis (2,4,6-trimethylbenzoyl) phosphine oxide obtained from Sigma-Aldrich, was added to the fiber-matrix mixture to initiate photopolymerization.

The carbon fiber reinforced UV curable was formulated by adding varying quantities of the fibers, matrix and initiator and mixed in a high energy ball mill at 1000 RPM for 30 mins to ensure uniform mixing of the fibers and matrix. The schematic for this has been shown in section 2.3. Although the Rigid resin already has an initiator, its effect is weakened by the presence of carbon fibers. Hence further initiator is added to the CFRP resin. The quantity of the initiator added is equal to 3% by weight of Rigid resin. Table 3.1 shows the quantities of different constituents required to obtain the CFRP resin with the required fiber loading.

Table 3.1: Formulation of the UV curable CFRP with different fiber loadings.

Fiber loading [vol%]	Weight of carbon fiber [g]	Volume of matrix [ml]	Weight of initiator [g]
5	4.45	47.5	1.71
10	8.9	45	1.62
20	17.8	40	1.44

Ball milling is done at 1000 rpm for 30 minutes to ensure uniform mixing of the fibers, matrix and initiator. However, this procedure has an effect on the length of the carbon fibers. Since the fiber length plays an important role in the outcome of its mechanical properties, the change in length of carbon fibers after the process was determined. The resin mixture was ball milled and a small quantity of the milled CFRP resin was observed under an optical microscope. Using cluster sampling technique, the length of all fibers in a certain region was determined using the ZEN imaging software by ZEISS and their distribution was plotted as shown in Fig. 3.1.

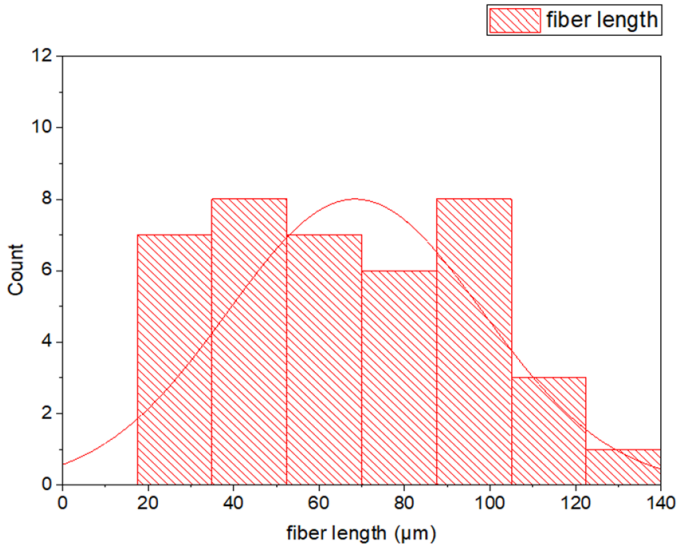

Figure 3.1. The distribution of fiber lengths after ball milling.

It is seen that the average length of the fibers was found to be 68.5 microns with a standard deviation of 29.8 microns. This value was lower than the value claimed by the carbon fiber manufacturer. Also, it was seen that the length decreased linearly with the increase in milling time.

Since the ultimate goal of this work is to design a lightweight microlattice with high stiffness and high damping, the stiffness and tan δ of material with high loss coefficient were also tested. Elastomers were the preferred choice of material to obtain high values of tan δ. After testing the loss coefficient of several elastomers, the Flexible resin developed by Formlabs Inc. was chosen because it provided the highest value of loss coefficient, making it ideal for this study. The Flexible resin is a mixture of acrylate oligomers, acrylate monomers and photo-initiators. It has a stiffness of 15MPa as reported by Formlabs Inc.

All the samples printed for the tests were post-cured under UV light for 1 hour followed by thermal curing at 200 °F for 24 hours to ensure effective curing. The printing parameters like curing time and UV light intensity were however increased with an increase in fiber loading.

3.3. Methods

The samples tested include pure Rigid resin (0% CFRP), 5% CFRP and 10% CFRP. All samples were tested in the XYdirection of the print. This ensures that failure does not occur due to layer debonding. This also ensured that the fibers are aligned in the XY plane. The direction of printing and testing is of importance because the properties of fiber-reinforced composites depend both on the direction of the fibers and direction of printing. Since fiber-reinforced composites behave differently in tension and compression, the modulus in both these loading conditions was tested. The mechanical loss coefficient of the composite was also tested. The results from these tests are used in the design of the high stiffness and high damping microlattice described in chapter 4.

To determine the tensile mechanical properties of the 3D printed samples, ASTM standard tensile test samples were fabricated and tested. The tensile tests were done on an Instron 5944 equipped with Bluehill data acquisition software and a 2000N load cell. Unidirectional tensile tests were performed to evaluate the stress-strain curve of the unit cell and determine the Young's modulus. A strain rate of $10^{-3}/s$ was employed on each sample until fracture. A total of 5 samples per volume fraction were tested to determine the modulus. The ASTM standard used for the test was ASTM designation – D3039 (Standard Test Method for Tensile Properties of Polymer Matrix

Composite Materials). Similarly, compression tests were performed using samples complying ASTM designation – E198 (Standard Test Method of Static Tests of Lumber in Structural Sizes, Section 13). The above standard was obtained from ASTM designation – E2954 (Standard Test Method for Axial Compression Test of Reinforced Plastic and Polymer Matrix Composite Vertical Members) for short structures. Shear tests were performed using cylindrical samples of 0.5" diameter and 2" length.

To determine the mechanical loss coefficient of the samples, a TA Instruments DMA 850 setup was used. The sample was loaded on the tension clamp and a strain sweep was performed from 0.1% - 1% strain. The goal of this was to determine the elastic limit of the sample. The strain within the elastic limit, as determined in the strain sweep, is used to run the frequency sweep from 0.1 Hz to 20 Hz. The lower limit of the test was chosen to determine the mechanical loss coefficient at near quasi-static loading rate and the upper limit was arbitrarily chosen to keep the test within a reasonable time duration. It is worth noting that the frequency range chosen would depend on the application the material is being chosen for. All tests were performed at room temperature (25 °C). This too can be changed depending on the application. Figure 3.2 shows a sample being tested using a tension clamp.

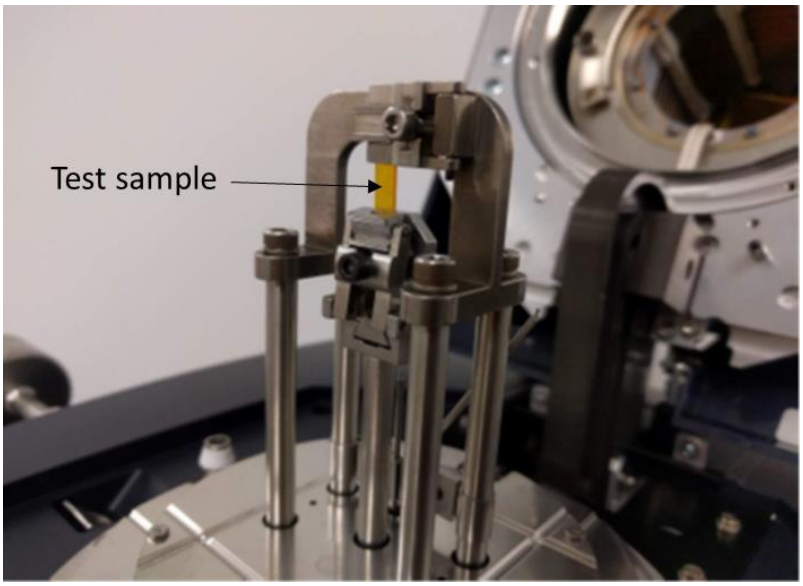

Figure 3.2. DMA test setup to determine the mechanical loss coefficient (tan δ) of the sample.

3.4. Results

3.4.1. Modulus tests

Figures 3.3, 3.4 and 3.5 show the test results for tensile, compressive and shear modulus respectively. The modulus is plotted against different volume fractions of carbon fibers loaded in the matrix resin. The red diamond in each plot represents the average value from the 5 samples that were tested and the error bars are positioned at one standard deviation. It is seen that the addition of carbon fibers to the matrix increased the modulus in all three cases. The tensile modulus of the pure matrix (without CF reinforcement) measured was slightly lower than the modulus claimed by Formlabs Inc. on their website. This can be attributed to the change in printing systems, printing parameters and post-curing techniques. The tensile modulus increased linearly with an increase in CF loading.

The compressive modulus too increases linearly with an increase in fiber loading. However, the stiffness in this direction is lower than the tensile modulus measurements due to the anisotropy in of fiber-reinforced composites. This is because, fibers under compressive loading fail via buckling, making them less stiff. It is also seen that the error bars in all cases are close to the average value. This suggests that the stiffness in the compressive direction in less susceptible to 3D printing defects such as porosity and layer adhesion. These defects were particularly evident in the measurement of shear modulus tests as can be seen in fig. 3.5. As the volume fraction increases, the shear modulus too increases more or less linearly. However, these measurements were prone to large errors due to print quality.

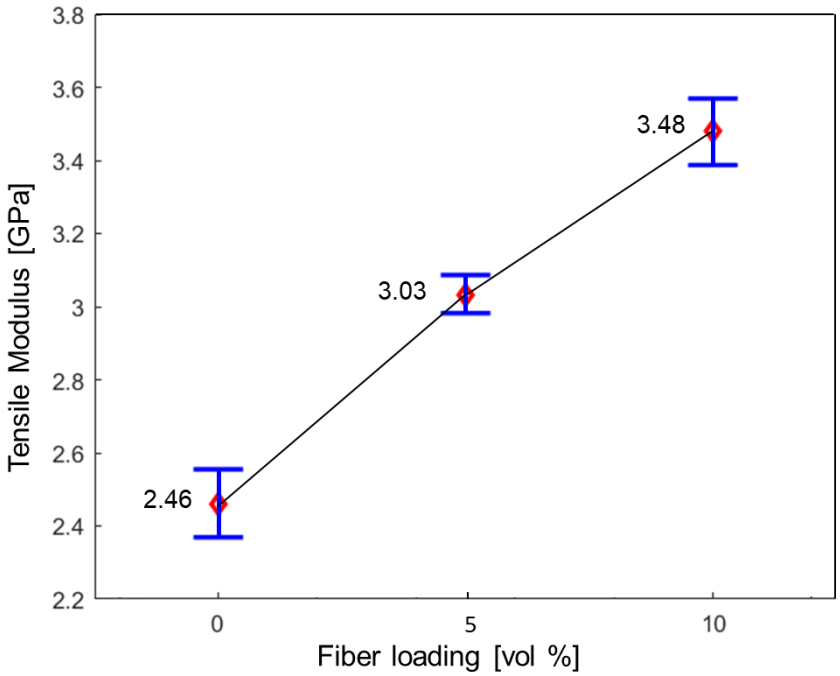

Figure 3.3. Experimental results from the tensile test.

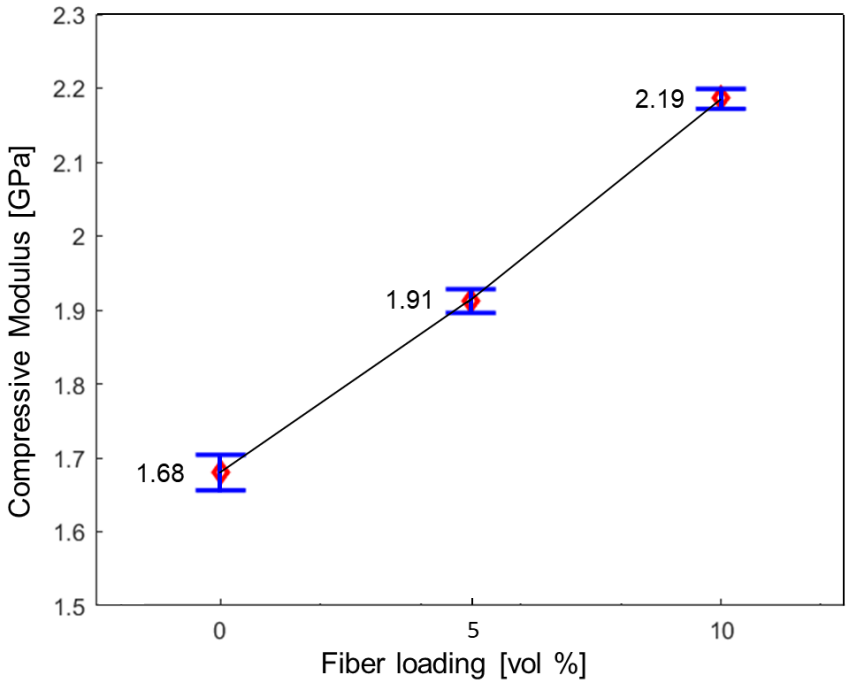

Figure 3.4. Experimental results from the compressive test.

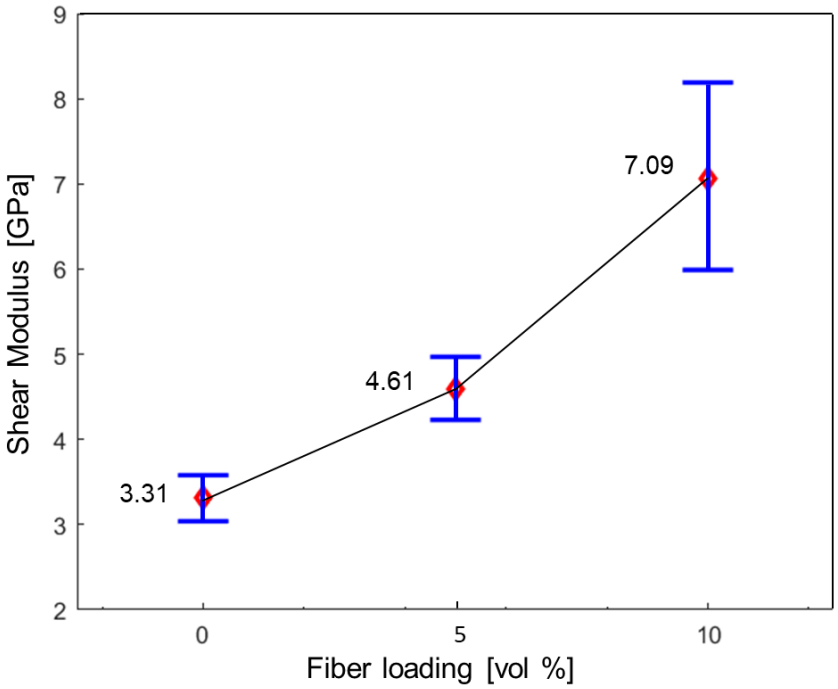

Figure 3.5. Experimental results from the shear test.

3.4.2. Dynamic tests

The results from the dynamic test are shown in Fig. 3.6. The curves show the tan δ values of different specimens under dynamic loading for a frequency range of 0.1Hz to 20Hz. The Rigid resin and 5% CFRP resin have high stiffness but low tan δ. The Rigid resin has a tan δ value of 0.098 at 0.1Hz, which decreases to 0.077 at 20Hz. Pure carbon fibers have a reported tan δ value of 1E-05. Hence, the addition of a small quantity of CF to the matrix reduces the tan δ value of the composite. There is no significant difference in the tan δ value of 5% and 10% CFRP composite and hence, only the 5% CFRP composite is represented to maintain figure clarity. Both the Rigid resin and the CFRP composite have near-constant values of tan δ over the chosen frequency range suggesting elastic behavior. The matrix material used for CFRP composite is the Rigid resin.

The Flexible resin exhibits high values of tan δ, increasing from 0.299 at 0.1Hz to a maximum of 0.872 at 10Hz and then gradually decreasing to 0.852 at 20Hz. The fluctuation in tan δ values indicates the viscoelastic behavior of this material in the given frequency range.

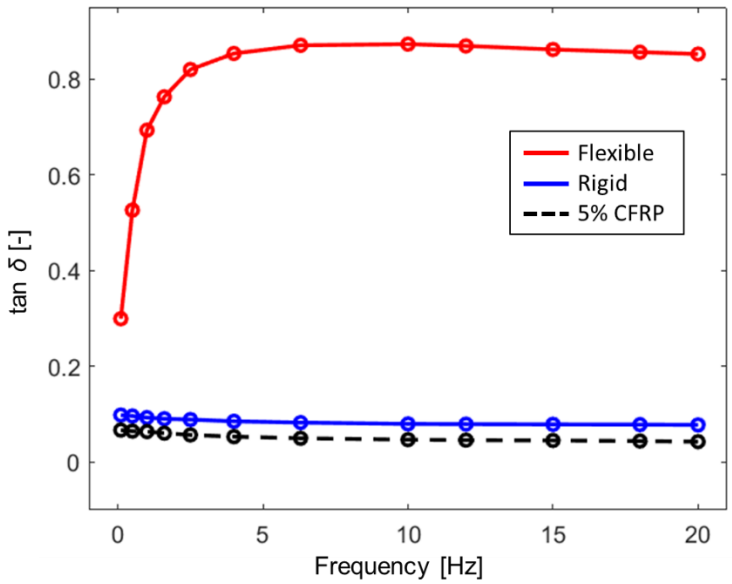

Figure 3.6. Experimental results for the mechanical loss coefficient from DMA tests.

3.5. Conclusion

CFRP samples with different fiber loading were fabricated and tested for stiffness and damping. It is seen that the stiffness in the tensile, compressive and shear directions increases linearly with increase in fiber volume fraction. This, however, was only proved at low volume fractions of CF. As the volume fraction increases, the print quality visually diminished due to difficulty in the 3D printing of CFRP composites using SLA. As a result, the improvement in properties of 3D printed CFRP composite at high volume fractions cannot be guaranteed unless the SLA system is improved.

3.6. Discussion

As shown in Fig. 3.7, when compared to the theoretical bounds as given by Eq. 3.1 and 3.2, the printed samples tested were close to the lower Reuss bound. This could be attributed to several factors. The upper Voigt bound assumes an ideal case of continuous fiber reinforcement in the sample, perfect alignment and perfect fiber-matrix adhesion. This is not the case in the samples tested. The fibers used for reinforcement as short and discontinuous. Despite the use of tape casting recoating technique, it is not possible to achieve perfect fiber alignment. Also, since the fibers are

not sized, there could be slippage between the fiber and matrix. All these factors result in the stiffness being closer to the lower bound. These factors also provide methods to improve the stiffness and reach closer to the upper bound. However, the results obtained show higher values of stiffness when compared to other studies using SLA and FFF techniques to 3D print CFRP composites [31] [32].

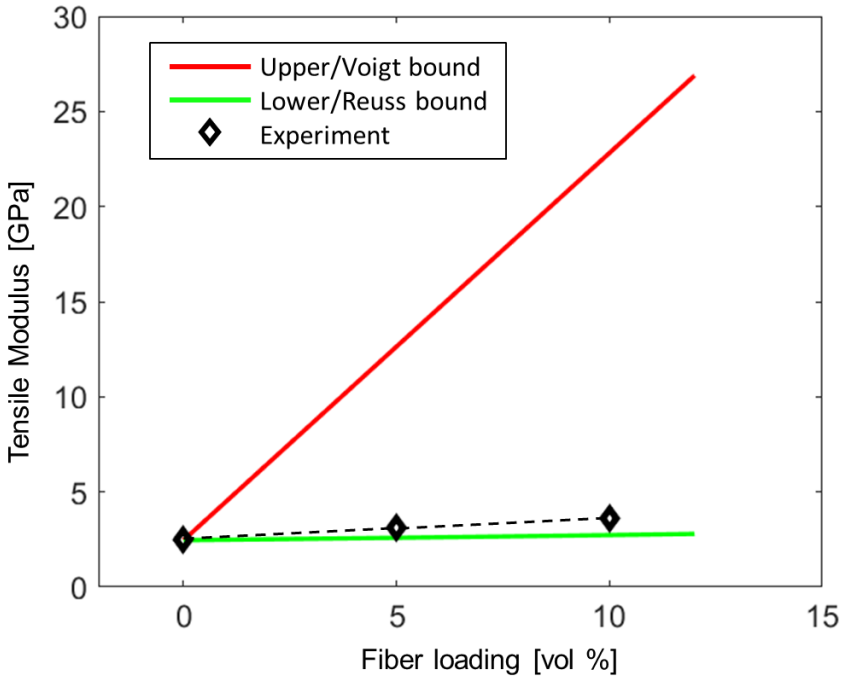

Figure 3.7. Comparison of the tensile modulus test results with theoretical bounds.

Although carbon fibers help increase the stiffness of the base matrix, it has an adverse effect on the mechanical loss coefficient or tan δ of the composite. The addition of fibers makes the composite perform poorly in terms of vibration damping, restricting its application in structural components where vibration damping is essential. On the other hand, the elastomer tested shows high damping and viscoelastic behavior. Using this result, a microlattice with a combination of these two materials for improved stiffness and damping is described in the next chapter.

Chapter 4: Analysis of viscoelastic composites

4.1. Introduction

Carbon fiber reinforced composites are known for their high stiffness-to-weight ratio. However, they have a low mechanical loss coefficient (tan δ), resulting in poor vibration damping. Chen at al. [33] reported that the addition of a high loss phase (referred to as soft phase from here on) to stiff phase in a two-phase configuration can lead to a high stiffness-loss pair. In this chapter, the use of such high loss materials along with CFRP composites in order to increase the tan δ and vibration damping in CFRP composites while having minimal effect on the stiffness is studied. The figure of merit of concern in this study is presented. The different types of damping mechanisms are studied and several viscoelastic composites for maximizing the FOM are analyzed.

4.2. Figure of merit

This section describes the choice of the figure of merit chosen. Figure of merit (FOM) can be defined as a quantity used to characterize the performance of a given material in order to enable comparison with its alternatives. The stiffness and tan δ of material are conflicting in nature. An increase in one usually results in a decrease in the other. As a result, it is important to quantify the performance using an FOM in order to measure the improvement as well as compare with other materials. In this study, the goal is to design a CFRP structure with lightweight, high stiffness and high damping. As a result, the parameters of concern in the FOM are relative density (ρ), Young's modulus (E) and mechanical loss coefficient (tan δ). It is important to realize that the figure of merit depends on the application of the material. In this case, the use of CFRP composites as panels in the automotive or aerospace industry is considered as the most likely application. Such applications require the material to be lightweight while having high stiffness and high vibration damping. In order to derive the FOM, let us consider a rectangular plate with area A, thickness t and material density ρ. The mass of the plate can be defined as –

$m = \rho A t$	(4.1)

The flexural rigidity of the plate, *R*, can be defined as –

$$R = \frac{Et^3}{12(1-\nu^2)} \quad (4.2)$$

Where E is the Young's modulus of the plate and ν is the Poisson's ratio. Solving for *t* in equation 4.2, we get –

$$t = \left(\frac{12R(1-\nu^2)}{E}\right)^{1/3} \quad (4.3)$$

Substituting *t* in eq. 4.1,

$$m = \rho A\left(\frac{12R(1-\nu^2)}{E}\right)^{1/3} \quad (4.4)$$

Eq. 4.4 can be grouped into constants, geometric parameters and material properties. Since ν is nearly the same for all structural materials, it is considered as a constant in the derivation of the figure of merit. After grouping, the mass *m* can be defined as –

$$m = \left(12(1-\nu^2)^{1/3}\right).\left(AR^{1/3}\right).\left(\frac{\rho}{E^{1/3}}\right) \quad (4.5)$$

Hence the figure of merit, M_1, to maximize stiffness and minimize the mass of a rectangular plate is defined as –

$$M_1 = \left(\frac{E^{1/3}}{\rho}\right) \quad (4.6)$$

Since our application also requires high damping, another figure of merit (M_2) is defined to maximize the damping or tan δ of the material.

$M_2 = \tan\delta$	(4.7)

The two figures of merit, M_1 and M_2 can be directly multiplied to obtain our desired figure of merit M for lightweight, high stiffness and high damping material for plate applications.

$M = \frac{E^{1/3} tan\delta}{\rho}$	(4.8)

The material with the highest value of FOM, M, is the best choice for lightweight, high stiffness and high damping panel. However, it must be noted that in this figure of merit, all three material properties (E, ρ and tan δ) play an equal role in selecting the material. If the designer needs to concentrate on one parameter more than the other, the penalty function approach can be used in which each parameter is weighted based on its relative importance. Also, it must be noted that the FOM for a truss or beam element with a similar application would be different.

4.3. Damping mechanisms

As seen in the previous section, tan δ plays the role in the FOM and hence in the quantifying of the performance of the lightweight, high stiffness and high damping design. As a result, it is necessary to understand the different damping mechanisms in lattice structures and ways to improve them. Salari-Sharif et al. [34] studied the damping or energy dissipation mechanisms in lattice structures under cyclic loading and classified them into several types. They include:

(i) Intrinsic material damping: It is the damping contributed by the properties of the material. It is observed at small strain, i.e., within the elastic limit.

(ii) Structural damping: Observed at large strains. It is caused by failure mechanisms like elastic buckling, plastic yield and fracture. Mechanisms like fracture and plastic yield largely disappear after the first few cycles.

(iii) Macroscale friction damping: It is caused by the frictional interactions between the lattice members when it is compressed.

(iv) Viscous damping: It is caused by the air present around the struts of the lattice, leading to energy loss.

(v) Microscale friction damping: Energy is dissipated by the small cracks and voids present in the lattice due to 3D printing. This is seen even at small strains.

Out of these five sources of damping, the major contributors in a lattice include intrinsic material damping and structural damping. Hence this chapter looks at ways to increase both of these damping mechanism contributions for CFRP composites. It must be noted that both these damping mechanisms are independent of each other and are observed at different strain and frequency regimes. However, for the purpose of this study, they are studied together to determine the combined damping property of the CFRP microlattice structure.

4.3.1. Intrinsic material damping

Intrinsic material damping is associated with the material behavior. It an important quantity to be considered while selecting materials for structural applications. It represents how effectively vibrations are dissipated within the material. A number of mechanisms are responsible for the dissipation of vibrational energy within materials and are different in different families of materials. The damping in photo-cured polymers is attributed to the sliding and rotation of long polymer chains, whereas, damping in metals is due to the movement of point or line defects [4]. However, most published information is empirical in nature and the underlying physical phenomena are not completely understood.

The loss tangent (tan δ) is a quantity used to empirically determine the intrinsic material damping of a material. Carbon fibers have low tan δ of $1x10^{-4}$ and thus have poor intrinsic damping. Consequently, CFRP composites too have too tan δ and intrinsic damping. On the other hand, viscoelastic materials like elastomers have high tan δ and provide good damping. To improve the damping of CFRP composites, two-phase hybrid materials consisting of CFRP composites and elastomers, wherein both stiffness and damping can be improved, are studied. The goal is to obtain a material with maximum stiffness-damping pair.

To realize this idea for CFRP composites, several two-phase configurations were studied. They include:

(i) Voigt composite: The two phases are arranged such that the strain in each phase is the same whereas the stress is additive.

(ii) Reuss composite: The two phases are arranged such that the stress in each phase is the same whereas the strains are additive.

(iii) Stiff fibers in soft matrix: Carbon fibers are added to a soft matrix.

(iv) Soft spheres in stiff matrix: The soft material is added to the CFRP composite.

(v) Hashin-Shtrikman composites: They are similar to the Reuss and Voigt composites for two-phase materials but have more conservative bounds.

The different two-phase configurations are represented schematically in Fig. 4.1.

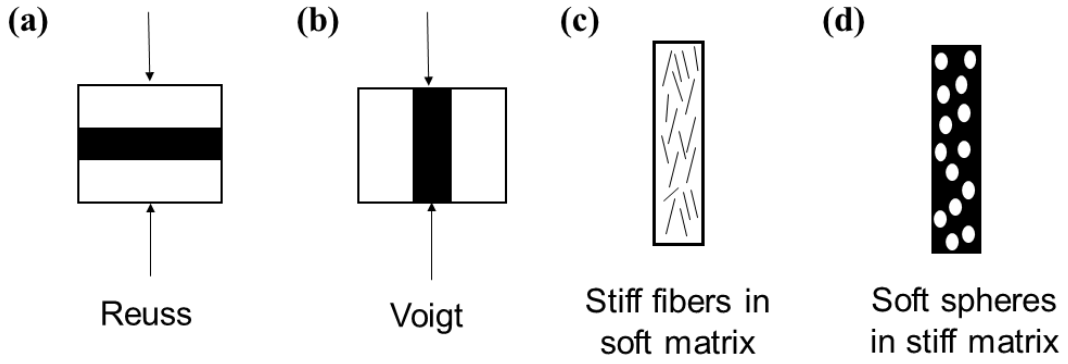

Figure 4.1. Schematic representation of the various two-phase composites studied.

To determine the effect of the stiffness-damping pair for each two-phase configuration, the theoretical variation of stiffness and tan δ with respect to the volume fraction of each phase is determined. In order to obtain this, let us consider a Voigt composite as shown in Fig. 4.1(b). Assuming that the material is elastic and there is no slip between the phases, Young's modulus is defined as –

$$E_c = E_{CF}V_{CF} + E_{soft}V_{soft} \quad (4.9)$$

In which E_c is the Young's modulus of the composite, E_{CF} is the Young's modulus of the CFRP composite, E_{soft} is the Young's modulus of the soft phase, V_{CF} is the volume fraction of the CFRP composite and V_{soft} is the volume fraction of the soft phase, such that $V_{CF} + V_{soft} = 1$. For

materials in the linear regime, the correspondence principle can be used to convert the elastic relation to a steady-state viscoelastic relation by replacing E by E^*. Thus, the viscoelastic or dynamic modulus of the Voigt composite is given by –

$$E_c^* = E_{CF}^* V_{CF} + E_{soft}^* V_{soft} \quad (4.10)$$

with $E_c^* = E_c' + iE_c''$, where E_c' is the storage modulus of the composite and E_c'' is the loss modulus of the composite. The loss tangent $\tan\delta = E_c''/E_c'$. For a perfectly elastic material, the stress and strain sinusoids are perfectly in phase and thus tan δ = 0 and as a result, the Young's modulus is equal to the storage modulus ($E_c^* = E_c'$).

Separating the real and imaginary parts form eq. 4.10, we get –

$$E_c' + iE_c'' = (E_{CF}' + iE_{CF}'')V_{CF} + (E_{soft}' + iE_{soft}'')V_{soft} \quad (4.11)$$

Real part:

$$E_c' = E_{CF}' V_{CF} + E_{soft}' V_{soft} \quad (4.12)$$

Imaginary part:

$$iE_c'' = i(E_{CF}'' V_{CF} + E_{soft}'' V_{soft}) \quad (4.13)$$

Taking the ratio of imaginary part to real part –

$$\frac{E_c''}{E_c'} = \frac{E_{CF}'' V_{CF} + E_{soft}'' V_{soft}}{E_{CF}' V_{CF} + E_{soft}' V_{soft}} \quad (4.14)$$

$$tan\ \delta_{Voigt} = \frac{V_{CF} tan\delta_{CF} + V_{soft} \frac{E_{soft}'}{E_{CF}'} tan\delta_{soft}}{V_{CF} + V_{soft} \frac{E_{soft}'}{E_{CF}'}} \quad (4.15)$$

Equations 4.9 and 4.15 can be used to plot the stiffness v/s tan δ values for Voigt composites over a range of volume fraction of the two-phases. Similarly, the Young's modulus for other two-phase composites mentioned earlier are given in equations 4.16-4.20 [35]. However, since the derivation of tan δ of these composites is complicated, it is done computationally and is only graphically represented in the stiffness-loss map shown in Fig 4.2.

Reuss -

$$\frac{1}{E_c} = \frac{V_{CF}}{E_{CF}} + \frac{V_{soft}}{E_{soft}} \quad (4.16)$$

Stiff fibers randomly oriented in a soft matrix –

$$E_c = \frac{1}{6} E_{CF} V_{CF} + E_{soft} \frac{1 + \frac{1}{4} V_{CF} + \frac{1}{6} V_{CF}^2}{1 - V_{CF}} \quad (4.17)$$

Soft spheres in stiff matrix –

$$E_c = E_{CF} - \frac{15(1 - \nu_{CF})(E_{CF} - E_{soft}) V_{soft}}{7 - 5\nu_{CF} + 2(4 - 5\nu_{CF}) \frac{E_{soft}}{E_{CF}}} \quad (4.18)$$

Hashin-Shtrikman lower –

$$E_c = E_{soft} + \frac{V_{CF}}{\frac{1}{E_{CF} - E_{soft}} + \frac{6(K_{soft} + 2E_{soft}) V_{soft}}{5(3K_{soft} + 4E_{soft}) E_{soft}}} \quad (4.19)$$

Hashin-Shtrikman upper –

$$E_c = E_{CF} + \frac{V_{soft}}{\frac{1}{E_{soft} - E_{CF}} + \frac{6(K_{CF} + 2E_{CF}) V_{CF}}{5(3K_{CF} + 4E_{CF}) E_{CF}}} \quad (4.20)$$

Where K_{CF} and K_{soft} are the bulk modulus of the CFRP composite and soft phase respectively. These theoretical relationships are used to plot the stiffness-loss maps (E vs. tan δ) for the different two-phase composites under consideration. The map helps us determine which two-phase composite maximizes the stiffness-damping pair.

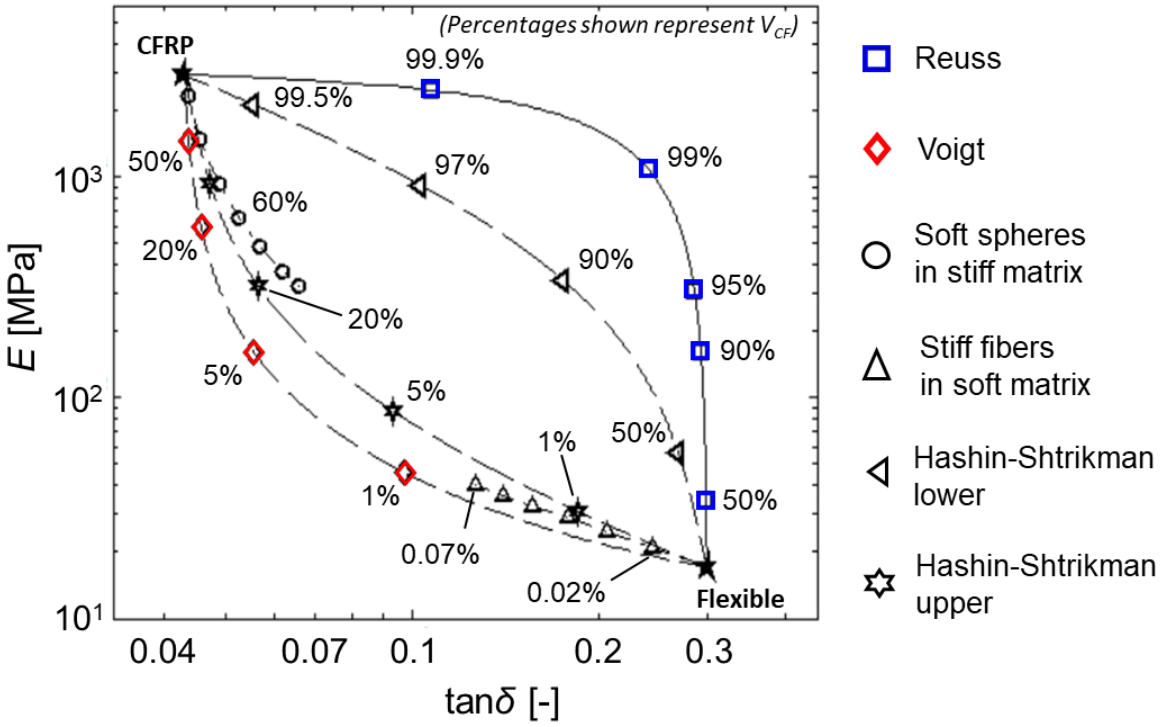

Figure 4.2. Stiffness-loss map for CFRP composites in various configurations obtained from theoretical predictions. It is seen that small addition of soft phase in Reuss configuration maximizes E - tan δ. The percentages shown in the map represent the theoretical volume fraction of stiff phase (CFRP)

The percentages represented in the stiffness-loss map represents the volume fraction of the stiff phase (CFRP). The values of stiffness and loss of CFRP and Flexible material represent the extreme values on the curve. The detailed procedure to determine these values can be seen in Chapter 3. The properties here are dynamic in nature and are represented for a frequency of 0.1Hz. The reason for choosing this specific frequency is explained in later sections.

From the figure, it can be seen that the Reuss curve occupies the top right area of the map, which is our target area since our goal is to maximize both stiffness and damping. The Voigt curve

occupies the lower left region of the curve and hence is not suitable for our purpose. The Reuss and Voigt curves form the bounds for stiffness-loss amongst the selected composite configurations. However, it must be noted that these are not the absolute bounds for stiffness-loss pairs. The upper and lower Hashin-Shtrikman composites behave similarly to Voigt and Reuss composites respectively but are conservative in nature. The addition of soft spheres in stiff matrix behaves similar to a Voigt composite. Also, the addition of stiff fibers to the soft matrix behaves like a Reuss composite in terms of increasing stiffness but there is no significant increase in the damping. Hence of the different configurations considered, it can be seen that Reuss composite gives the best stiffness-loss configuration.

From the plot, it can be seen that a small addition of the soft phase in Reuss configuration dramatically changes the stiffness-loss pair values. Figure 4.3 shows the variation of the FOM with the volume fraction of the soft phase for Reuss and Voigt composite. Only these two composites were chosen as they represent the bounds in our stiffness-loss map. It can be seen that for the given FOM, the Reuss composite always performs better than the Voigt composite. Also, a small addition of soft phase results in a dramatic increase in the FOM in the case of Reuss configuration. The FOM reaches a maximum at V_{soft} = 0.9% after which it gradually decreases. This trend is seen because the tan δ increases rapidly with a small addition of soft phase and reaches its maximum value. However, the stiffness continues to drop as the volume fraction of soft phase increases. From the figure, it can be concluded that for the given pair of soft and stiff composites, the addition of 0.9% of soft phase to CFRP in Reuss configuration can maximize the FOM.

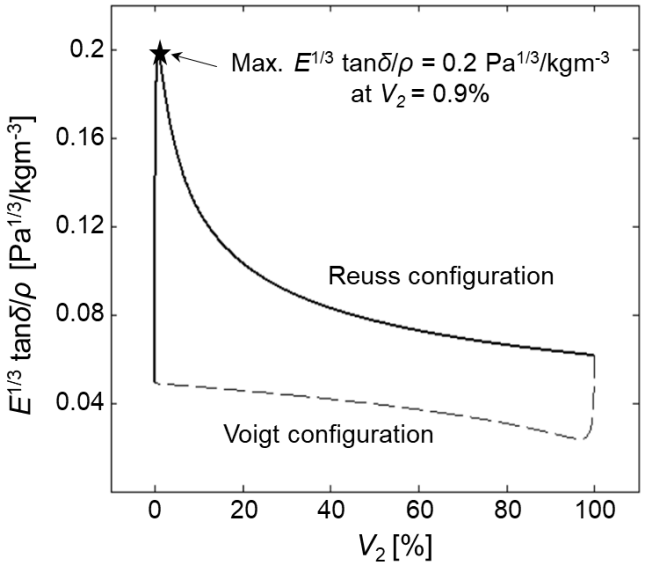

Figure 4.3. Variation of the FOM with the increase in the volume fraction of soft phase for Reuss and Voigt configurations.

Experiments were conducted to validate the theory and determine the volume fraction of soft phase required to maximize the FOM. Samples with Reuss configuration and 5%, 9%, 11%, 15% and 20% volume fraction of soft were fabricated using the SLA system and tested for stiffness and tan *δ.* As seen in Fig. 4.4, the experimental results were off the theoretical prediction by one order of magnitude. The experimental volume fraction to maximize the FOM was around 9% - 10%. Even after several repetitions of the test, the results were the same. This discrepancy was attributed to the fabrication defects during 3D printing. Since a multi-material system, as described in Chapter 2, is used to fabricate the samples, the transition between two different materials is not perfect and successive layers after the material change is contaminated by the previous material. Also, there could be problems in the adhesion of layers of two different materials. These defects are believed to be the cause of the discrepancy in theory and measurement. However, the experimental values follow the theoretical Reuss curve, giving us confidence in the work.

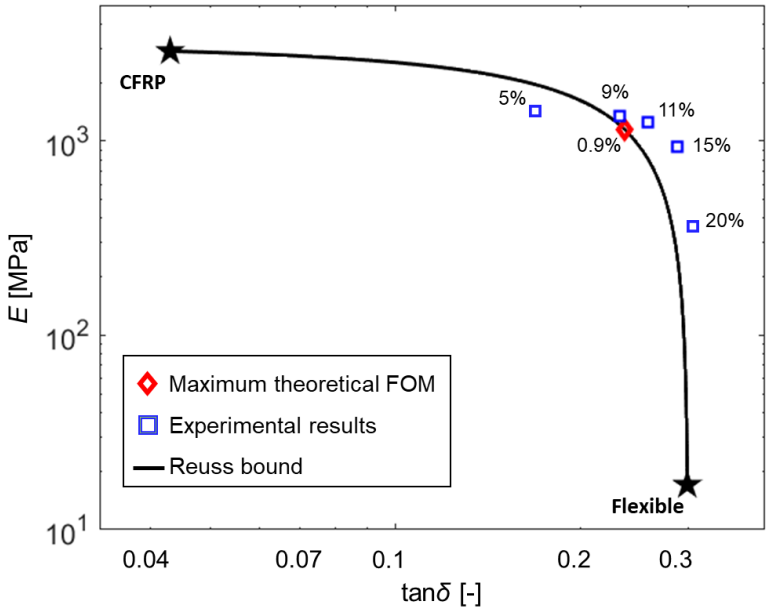

Figure 4.4. Plot comparing the theoretical and experimental values of V_{soft} to maximize the FOM.

All in all, it is experimentally seen that CFRP composite in Reuss configuration with 9% - 10% soft phase helps maximize the stiffness-loss pair. This section, however, only maximizes the intrinsic material damping of the CFRP composite. In the next section, the other major contributor, structural damping, is studied and a design to maximize the combined value of tan δ through both these mechanisms is presented.

Chapter 5: Design of lightweight, high stiffness and high damping microlattice

5.1. Introduction

While the characterizations from chapter 4 provide design guidelines for optimizing the stiffness-damping pairs of fully dense CFRP bulk samples, it remains elusive how these beneficial pairs can be translated to low-density regimes. Bulk CFRP structures, as studied until now, suffer from a low stiffness-to-weight ratio when compared to cellular structures. The density of the printed CFRP bulk samples is about 1230 kg/m^3. Cellular structures ranging from natural cellular materials such as bone and wood to human-made lightweight cellular materials such as honeycomb core give rise to a superior stiffness-weight relationship by virtue of their high stiffness and strength at low densities, several times lighter than water. Recently, applications incorporating the periodic cellular structures particularly in vibration damping have been studied [23] [24]. Moreover, studies have shown increases in the damping performance of the cellular materials through dissipative elements [25] and negative stiffness inclusions [26] [27]. Thus, for the purpose of designing a material incorporating high stiffness and damping and a beneficial stiffness-weight ratio of cellular materials simultaneously, a two-phase CFRP microlattice was developed. The performance of the design is quantified in terms of a figure of merit, $E^{1/3}\tan\delta/\rho$. The different types of damping mechanisms in the microlattice are studied. The design is experimentally tested and the results are compared with existing families of materials.

5.2. Damping in cellular structures

Apart from a superior stiffness to weight ratio, cellular structures also add to the structural damping of the design. Structural damping is an energy dissipation mechanism seen at large strains, due to the deformation of the sample. Failure modes like fracture, plastic work, elastic buckling are contributors to structural damping. Structural damping is dependent on the geometry of the structure and is measured by subjecting the structure to cyclic compressive loading. Details of this procedure are described in later sections. In this study, in order to maximize the structural damping and stiffness at low densities simultaneously, an octet-truss topology is chosen as the unit cell of the microlattice because of its stretching-dominated nature and its higher stiffness-to-weight ratio

(i.e., E/ρ) when compared to other truss topologies. However, it must be noted that there are other unit cells with a higher stiffness-to-weight ratio [36]. The octet truss is chosen over the closed-cell foams as it is easier to print and has been previously well studied [37]. Octet truss unit cell topology is also known to tend to fail under buckling at low relative densities [38], ideal mechanism for improved structural damping.

5.3. FE analysis of octet truss

In order to determine the stress and deformation fields in the octet truss unit cell, an FE analysis was performed. First, a CAD model of the unit cell was generated and the outside phases were flattened out in order to make them flat surfaces and enable load application. The CAD file is imported into the Abaqus software package to run the FE analysis. In order to mimic the behavior of the octet truss unit cell under compression, reference points were created in the center of the top and bottom phase. These reference points were coupled in all degrees of freedom to the top and bottom faces respectively to ensure that they move as one. Prescribed displacements of equal magnitude and opposite direction were defined on the top and bottom reference points. Because of the complex design of the structure, a 3D stress 10-node quadratic tetrahedron, C3D10, element was used.

Figure 5.1 shows the stress distribution in the octet truss unit cell under compressive loading. It is seen that the maximum stress is observed at the nodes, where the struts meet. This result could be attributed to the stress concentration in these regions. It is also seen that the out of plane struts of the octet truss are under higher stress when compared to the in-plane struts. Also, upon closer observation, it is seen that the out of plane struts deform in their first mode, i.e., the deformation is maximum at the center of the struts. This result was backed up by experimental observation. These FE results, along with experimental observations, help identify regions where soft phase needs to be added to maximize the allowable strain in the structure. It was concluded the addition of soft phase at the center of the out-of-plane struts best achieves this goal.

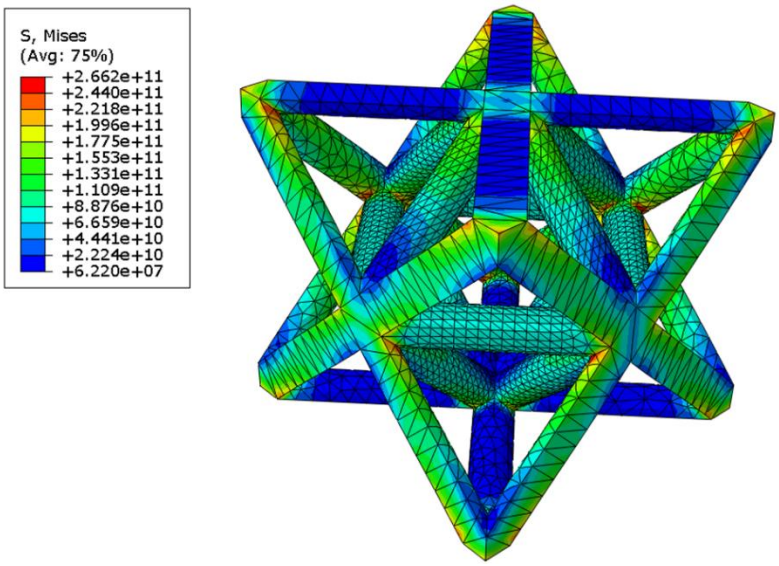

Figure 5.1. FE analysis of octet truss unit cell showing the stress distribution.

It must be noted that topology optimization can be used to determine the best distribution to maximize the figure of merit. However, that is beyond the scope of this work.

5.4. Design for maximizing FOM

A lattice structure with octet truss unit cell to maximize the intrinsic damping, structural damping and stiffness at low densities, and thereby the FOM, is presented in Fig. 5.2. It consists of multiple octet-truss unit cells made of CFRP composite. The soft phase is present in select out-of-plane struts in such a way that it is embedded at the center of these struts where the maximum deformation occurs as seen in the FE analysis shown earlier. This addition allows for an increase in the global strain of the microlattice and produces a larger enclosed area in the stress-strain hysteresis loop upon cyclic loading, leading to enhanced energy dissipation through structural damping. Furthermore, this lightweight cellular CFRP microlattice design is expected to behave like a Reuss structure when loaded in the longitudinal direction. It is also seen that the interface between the CFRP and the soft phase was found to be adequately strong to transfer tensile and compression loads between the two phases. These were verified through experimental observations. A scanning electron microscope (SEM) image was taken at the boundary, as shown in Fig. 5.2(c), displays a desired separation between the two phases. In this figure, the upper region is CFRP whereas the soft phase is in the lower region.

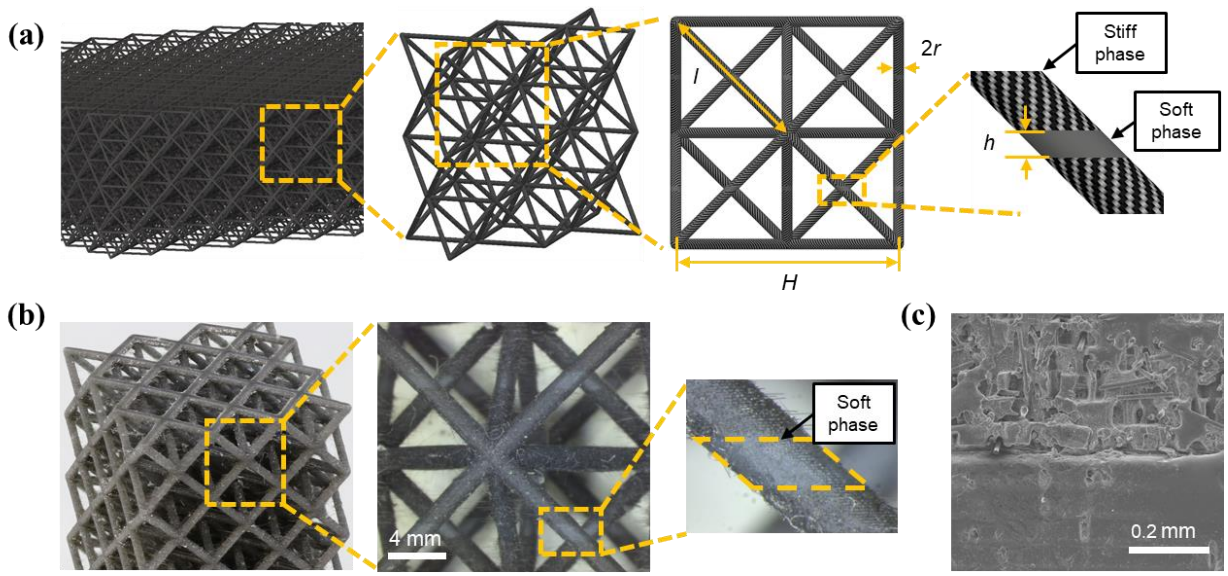

Figure 5.2. Multi-material architecture. (a) Design of lightweight, stiff, high damping microlattice with two-phase materials incorporating CFRP and soft phase. (b) Fabricated lightweight cellular CFRP microlattice having $\bar{\rho}$ = 7% with V_{soft} = 9%. (c) SEM image showing the interface between the two phases.

The geometric parameters for fully describing the presented microlattice are the relative density, $\bar{\rho}$, the thickness of the soft phase, h, and the edge length of the cell, H. The relative density of the octet-truss unit cell is defined as $\bar{\rho} = 6\pi\sqrt{2}(r/l)^2$, where r is the strut radius and l is the length of each strut [37]. This parameter governs the effective stiffness of the structure. The soft phase ratio in a single Reuss strut, V_{soft}, defined as the ratio of h to H, controls the volumetric material distribution between the CFRP and the soft phase, which essentially tailors the stiffness-damping property of the structure. Again, not all struts of the unit cell have soft phase embedded in them. The out-of-plane struts having Reuss configuration are only those that are orthogonal to the compressive loading. This was an informed decision made to significantly reduce print times. The V_{soft} is related to the volume fraction of the soft phase to the entire microlattice's soft phase volume as $V_{soft}^{lattice} = (2/3)V_{soft}$.

In order to investigate the performance of the stiffness-damping pair of the present microlattice, several samples were fabricated using the multi-material PμSL described earlier. Microlattices

having the relative densities, $\bar{\rho}$, of 4%, 7%, 12% with the soft phase ratio, V_{soft}, of 0%, 5%, 9%, 13%, 20%. In Fig. 5.2(b), a representative lattice microstructure having a relative density of 7% with V_{soft} of 9% is shown. The specific relative densities were chosen to capture damping due to buckling and non-buckling behavior. 4% relative density was chosen as it represents the lower limit of the fabrication capability of the system. 7% and 12% relative densities were chosen to differentiate the damping behaviors at different relative densities while keeping the design in the low-density regime. Also, the volume fraction of soft phase was chosen to capture the peak FOM due to intrinsic material damping, seen at 9%-10% in the earlier sections.

5.5. Investigation of damping performance of microlattice

5.5.1. Intrinsic damping

The intrinsic and structural damping of the microlattice were experimentally investigated individually and later coupled to determine the total effective damping of the microlattice. In this study, the microlattice is viewed as a material in the context of continuum mechanics when it is composed of a sufficiently large number of cells. To capture intrinsic damping properties of the lightweight cellular CFRP microlattice, small strain DMA tests were performed on the unit cell of the microlattice using the TA Instruments DMA 850. The samples were compressed dynamically from a frequency of 0.1Hz to 20Hz and at a strain of 0.05% to ensure that the excitation was within the elastic behavior of the sample. It is assumed that the unit cell is representative of the intrinsic material damping of the microlattice. Although a range of frequency sweep was from 0.1 Hz to 20 Hz, the results measured at 0.1 Hz were adopted in this study because the resulting loss tangent, tan δ, allows for a direct comparison with damping property obtained from small-strain DMA and quasi-static large-strain experiments. It is worth noting that loss tangent, tan δ, can be measured at higher frequencies to determine the suitability of the material for vibration isolation in specific applications like jet engines, helicopter gears, golf clubs. [35].

The intrinsic damping of the unit cell having a relative density of 7% with various volume fractions of soft phase (i.e., 0%, 5%, 9%, 13%, and 20%) was studied. A single relative density was considered for a study of intrinsic damping because it can be theoretically proven (shown below)

that the intrinsic damping for cellular structures is only dependent upon the material distribution and not on geometric relationships such as a relative density.

Let us consider an octet truss with relative density, $\bar{\rho}$. According to Deshpande et al. [37], the effective stiffness, E_s, of the octet truss unit cell made of struts comprised of a material with stiffness E can be defined as –

$$E_s = \frac{\bar{\rho}}{9} E \tag{4.21}$$

Since, in the current design, the struts are made of Reuss configuration, the effective stiffness of can be defined as –

$$E_s = \frac{\bar{\rho}}{9} E_{Reuss} \tag{4.22}$$

Using the correspondence principle, the elastic equation can be converted to its complex form.

$$E_s^* = \frac{\bar{\rho}}{9} E_{Reuss}^* \tag{4.23}$$

We know that $\tan\delta = E''/E'$. Solving for tan δ in equation 4.23, we obtain,

$$tan\ \delta_S = \frac{(tan\delta_{CF} + tan\delta_{soft})(V_{CF} + V_{soft}\frac{E'_{soft}}{E'_{CF}}) - (1 - tan\delta_{CF}tan\delta_{soft})(V_{CF}tan\delta_{soft} + V_{soft}tan\delta_{CF}\frac{E'_{CF}}{E'_{soft}})}{(1 - tan\delta_{CF}tan\delta_{soft})\left(V_{CF} + V_{soft}\frac{E'_{soft}}{E'_{CF}}\right) + (tan\delta_{CF} + tan\delta_{soft})(V_{CF}tan\delta_{soft} + V_{soft}tan\delta_{CF}\frac{E'_{CF}}{E'_{soft}})} \tag{4.24}$$

$$tan\ \delta_S = tan\ \delta_{Reuss} \tag{4.24}$$

From equation 4.24 it can be seen that the tan δ of the lattice is not a function of the relative density. It only depends on the material distribution. To note, here, it is assumed that all the struts of the unit cell are of Reuss configuration, which is not true in our case. However, this assumption can be made since we are only concerned with the dependency of tan δ on the relative density of the unit cell and not used for determining any values analytically.

Figure 5.3(a) and 5.3(b) show the effective modulus (i.e. storage modulus) and tan δ of the unit cell respectively. The results were obtained from the DMA test of the samples at 0.1 Hz. The values are also listed in table 5.1. The storage modulus represents the stiffness of the structure at that frequency. The results indicate that the effective modulus of the samples is inversely proportional to V_{soft} and follows an exponential relationship as a function of V_{soft} in such a way that $E = ae^{bV_{\text{soft}}} + ce^{dV_{\text{soft}}}$. This physically makes sense because a sample with a higher V_{soft} would be governed by the elastic behavior of the soft phase. Conversely, it appears that loss tangent (tan δ), which represents intrinsic damping, is nonlinearly proportional to V_{soft} in a sense that $\tan\delta = ae^{bV_{\text{soft}}} + c$. This curve fit predicts an asymptotic value of the loss tangent to be approximately 0.33 which in fact corresponds to the inherent loss tangent of the soft phase. Moreover, it is seen that the loss tangent is more sensitive to V_{soft} than the modulus because a small addition of the soft phase gives rise to a significant improvement of the loss tangent. Notice that these phenomena are similar to those observed from a study of the bulk materials performed in Section 4.3.1. The coefficients for the curve fit of effective modulus and tan δ are listed in table 5.2. The curve fits shown for storage modulus and loss tangent have an R^2 value of 1 and 0.95 respectively, indicating a good fit. It must be noted that in order to obtain a good fit for the loss tangent, its value at 50% volume fraction of soft phase was estimated at 0.33 since it reaches an asymptotic value. Also, the damping behavior is similar to bulk sample damping behavior as shown in Fig. 4.4. This is because the sample is excited at very small strains, capturing only the intrinsic material damping.

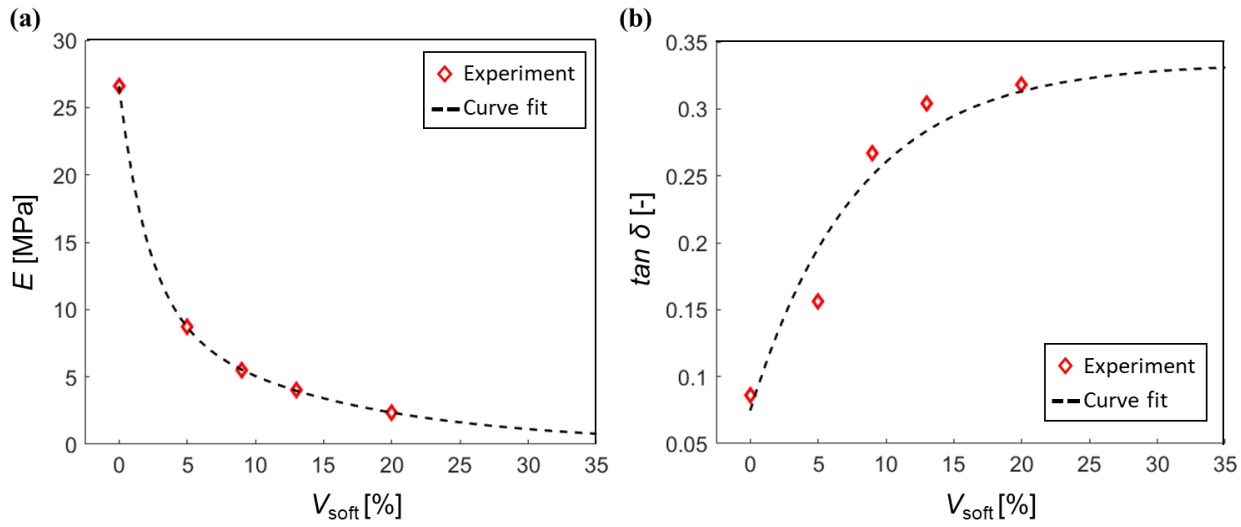

Figure 5.3. Intrinsic damping properties of a lightweight cellular CFRP microlattice having a relative density of 7 % with different volume fractions of soft phase. (a) The effective modulus (E) as a function of the soft phase ratio V_{soft}. (b) Loss tangent (tan δ) as a function of V_{soft}.

Table 5.1: Storage modulus (i.e. stiffness) and intrinsic tan δ of the samples with relative density of 7 % at small-strains.

V_{soft}	0%	5%	9%	13%	20%
Storage modulus [MPa]	27.060	9.323	6.130	4.108	2.659
tan δ [-]	0.086	0.156	0.267	0.304	0.318

Table 5.2: The coefficients of fitting equations of storage modulus (i.e. stiffness) and tan δ of the samples with relative density of 7 % at small-strains.

Coefficients	a	b	c	d	R^2
Effective modulus [MPa]	16.35	-0.4649	10.25	-0.0736	1
tan δ [-]	-0.2569	-0.1258	0.3341	N/A	0.95

For evaluating the performance of stiffness-damping pair, FOM is examined, as shown in Fig. 5.4. The dashed line represents a trend based on the fitted curve equation of the FOM, obtained from the results of the effective modulus and loss tangent. Results show that the addition of a small quantity of soft or high loss phase increases the FOM and it has its peak when V_{soft} is approximately equal to 13%. The FOM increases from 0.029 $Pa^{1/3}/kgm^{-3}$ for the CFRP microlattice to a maximum

value of 0.055 $Pa^{1/3}/kgm^{-3}$ at 13% V_{soft} and then decreases exponentially as the soft phase volume fraction increases further. This trend of the intrinsic stiffness-damping performance of the microlattice is similar to the bulk sample tested earlier. The finding indicates that the intrinsic stiffness-damping performance of the present microlattice is not only tailorable but also can be designed for maximal stiffness-damping material. Again, it must be noted that the stiffness and loss tangent values at 50% volume fraction of soft phase were estimated to obtain a more representative fit. The stiffness at 50% V_{soft} was estimated using the curve fit obtained from Fig. 5.3(a).

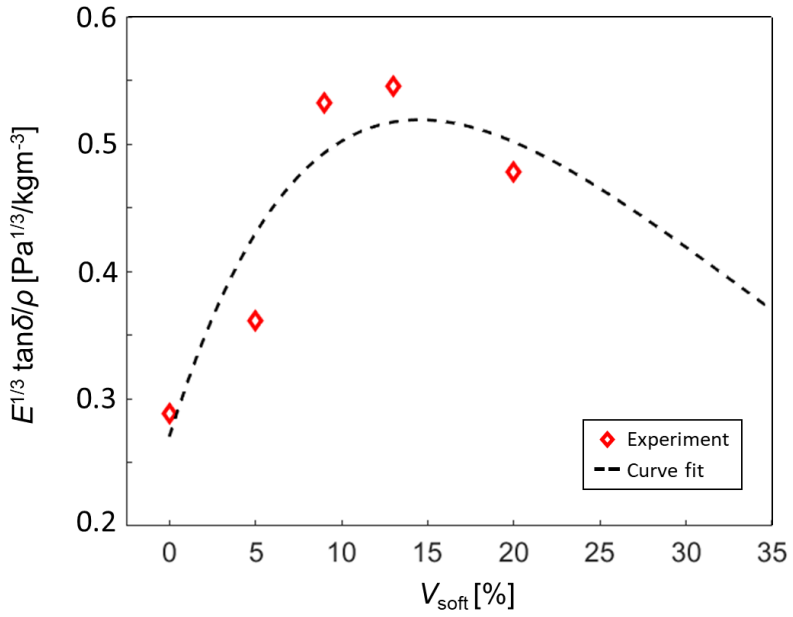

Figure 5.4. The intrinsic damping figure of merit as a function of V_{soft}.

In order to represent the FOM over a range of values of relative density of unit cell, $\bar{\rho}$ and volume fraction of soft phase, V_{soft}, a 2D map, as shown in Fig. 5.5, is presented. As described earlier, the FOM has its maximum at low relative densities and a volume fraction of around 13%. The curve fits obtained from the stiffness and loss tangent plots, shown earlier were used to generate the map. As the relative density of the microlattice increases, the loss tangent remains constant. However, the $E^{1/3}/\rho$ decreases, thereby reducing the FOM. The variation of FOM with volume fraction of soft phase has been described in earlier sections. It must be noted that this map only represents the

FOM with respect to the intrinsic damping of the material. Also, this theory can be extended to other types of unit cells as well. Any unit cell comprised of the same combination of materials and distribution would behave similarly.

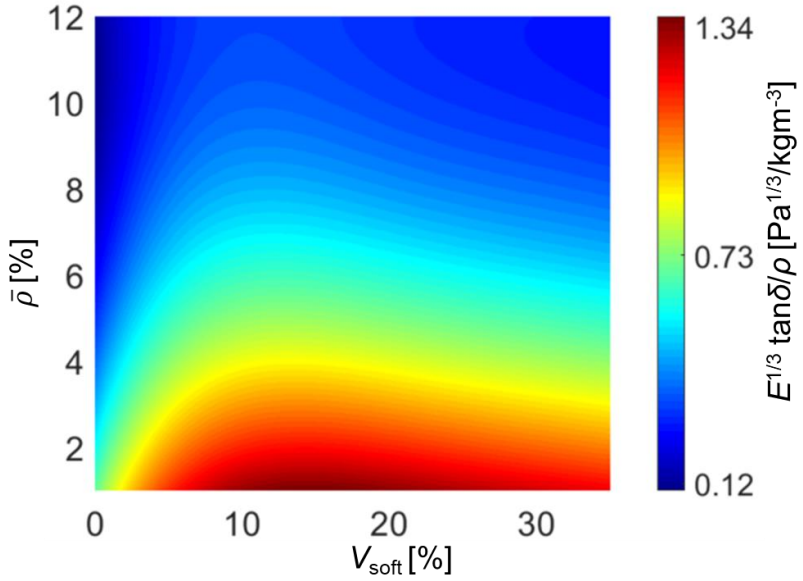

Figure 5.5. Tunability maps for intrinsic damping performance in terms of the figure of merit obtained from experimental measurements.

5.5.2. Structural damping

Until now, the intrinsic damping properties and FOM associated with it were studied. The properties were measured at small strains and the energy dissipation or damping was solely a factor of the materials and its distribution and independent of the topology. In this section, the energy dissipation of the design due to structural mechanisms like fracture, yield and buckling is studied. This damping mechanism, also referred to as structural damping is measured by subjecting the unit cell to cyclic loading.

The structural damping properties of the lightweight cellular CFRP microlattice were investigated by performing large-strain quasi-static cyclic compression tests using an INSTRON 5944 test frame equipped with Bluehill data acquisition software and a 2000 N load cell. For the cyclic

compression tests, a strain rate of 10^{-3}/s was adopted to ensure that all tests were performed in a quasi-static regime (to suppress mass inertia effect). Load-displacement curves were collected by the software linked to the test frame and were converted into engineering strain and stress as $\varepsilon = \delta/L_0$ and $\sigma = P/A$, where P and δ are the load and displacement measured by the load cell, respectively, L_0 is the initial length, A is the cross-section area.

The procedure to determine tan δ from cyclic tests is shown in Fig. 5.6. From the measured stress-strain hysteresis loop, the effective modulus was computed from the slope of a loading curve in the linear region. The dissipated energy (ΔU) was measured by calculating the area within the stress-strain hysteresis loop, and the stored energy (U) was measured from the area under the loading curve. The last two measures were used to evaluate the damping performance of the microlattice in terms of the loss coefficient (Ψ) defined as the ratio of the dissipated energy to the stored energy (i.e., $\Psi = \Delta U/U$) [34]. The loss coefficient is then converted to tan δ via $\Psi = (\pi/2)\tan\delta$ [4] [5]. This conversion allows for a direct comparison of tan δ from intrinsic and structural damping. Note that this conversion represents a quarter-cycle of a full cycle compressive loading-unloading response [5].

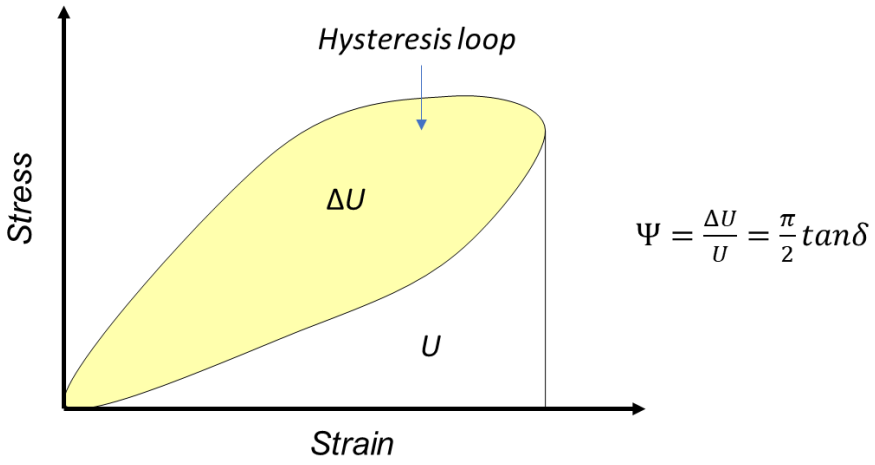

Figure 5.6. Schematic showing the procedure to obtain tan δ from the cyclic compression test.

Firstly, the response of the unit cell to multiple compression cycles was studied to understand the dominant energy dissipation mechanisms. Unit cells with $\bar{\rho}$ = 4% and $\bar{\rho}$ = 12% having V_{soft} = 20% were chosen and subjected to 30 compression cycles. The samples were loaded up to a strain just

before failure. The specific samples were chosen because the hysteresis loops from relative densities, $\bar{\rho}$ = 4% and $\bar{\rho}$ = 12% would be distinguishable and also V_{soft} = 20% allowed maximum strain during loading. The results from the cyclic tests are shown in Fig. 5.7(a) and (b). It is observed that the hysteresis loops stabilized after approximately 3 cycles. This could be attributed to the presence of non-recoverable mechanisms such as localized nodal fractures and possible inelastic deformation. Similarly, the loss coefficient decreases for up to 3 cycles (~25%). After 3 cycles, the is loss coefficient reaches a plateau region in which it is almost constant, indicating elastic energy dissipation mechanisms. It must be noted that in the plateau region, energy dissipation due to material properties, i.e. intrinsic material damping is also included. In other words, the structural damping obtained from cyclic compression of the sample has a contribution from intrinsic material damping.

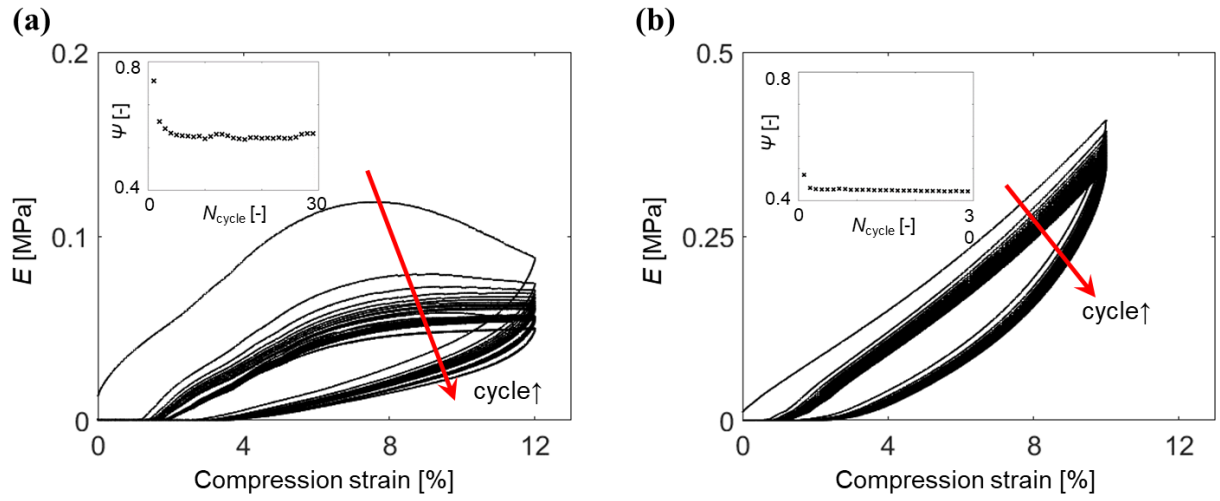

Figure 5.7. Hysteresis loops from multicyclic compression tests for 30 cycles and evolution of the loss coefficient with cycle number (inset). (a) Sample with $\bar{\rho}$ = 4% having V_{soft} = 20%. (b) Sample with $\bar{\rho}$ = 12% having V_{soft} = 20%.

Next, the effect of energy dissipation mechanisms at different relative densities, $\bar{\rho}$ = 4%, $\bar{\rho}$ = 7% and $\bar{\rho}$ = 12% was investigated. Again, the volume fraction of soft phase chosen was V_{soft} = 20% to enable maximum strain during cyclic compression. Since the loss coefficient of the samples levels out after 3 cycles, the results from the third cycle were used. Fig. 5.8 shows the evolution of the hysteresis curve for different relative densities. To clearly display the evolution, the curves were normalized for both stress and strain with respect to their maximum values. It was seen that the

dominant deformation mechanism at a low relative density ($\bar{\rho}$ = 4 %) was elastic buckling of the constituent struts. This is indicated by the negative slope in the stress-strain curve. As the relative density increases ($\bar{\rho}$ = 7 %), this buckling response diminishes and elastic compression mechanism starts to dominate at a higher relative density ($\bar{\rho}$ = 20 %). This difference in deformation mechanisms at different relative densities affects the shape of the stress-strain hysteresis loops that in turn leads to a change in the dissipated energy per cycle and structural damping. Due to the presence of buckling, the structural damping is maximum at low relative densities. As the relative density increases, the sample fractures before buckling.

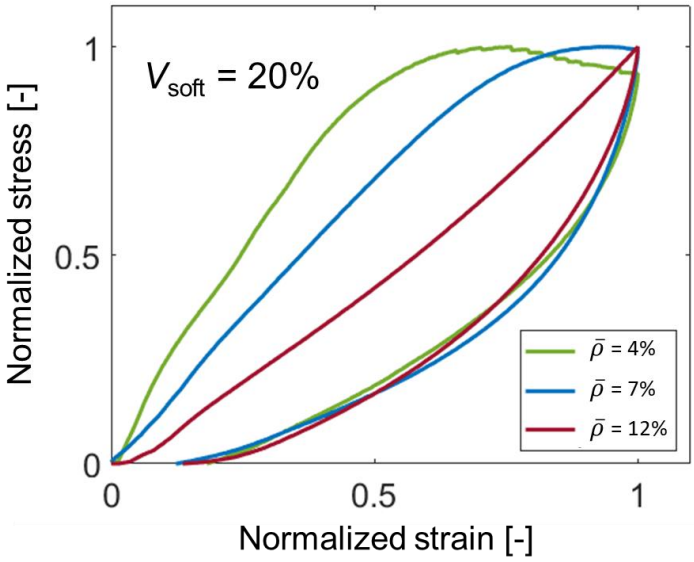

Figure 5.8. Normalized stress-strain hysteresis loops of samples having V_{soft} = 20% with various $\bar{\rho}$. Elastic buckling behavior was observed for $\bar{\rho}$ = 4% and diminished with an increase of $\bar{\rho}$ resulting in a reduction in the area of the loop.

To determine the stiffness, E, loss tangent, tan δ and thereby the FOM, all samples were subjected to cyclic compression tests. The values of E and tan δ are listed in tables 5.3. and 5.4. and their variation with respect to V_{soft} for different relative densities is summarized in Fig. 5.9(a) and 5.9(b). It is seen that the effective modulus of the microlattice was proportional to the increase in the relative density. This is consistent with other typical cellular structures since such structures exhibit a scaling relationship between the modulus and relative density. Additionally, for a given relative density, the modulus monotonically decreases with an increase in V_{soft}, and this

relationship is nearly identical to the behavior of the storage modulus observed in the intrinsic properties. As the volume fraction of the soft phase increases, the moduli of the different relative densities seem to converge. Curve fits for the measured modulus were found to follow an exponential relationship of V_{soft} such that $E = ae^{bV_{soft}} + ce^{dV_{soft}}$.

The structural damping response of the microlattice, loss tangent (tanδ), obtained via $\Psi = (\pi/2)\tan\delta$ where $\Psi = U/\Delta U$, is shown in Fig. 5.9(b). The results show that the (structural) loss tangent monotonically increases with V_{soft} and is inversely proportional to the increase in relative density. Additionally, with an increase in V_{soft}, the loss tangent of all samples reaches its asymptotic value, and this convergence is more rapid for samples with higher relative densities. The curve fit is described by the equation $\tan\delta = ae^{bV_{soft}} + c$. The coefficients of curve fit for modulus and tan δ are mentioned in tables 5.5 and 5.6 respectively. As mentioned earlier, a dominant deformation mechanism of samples at low relative densities (e.g., $\bar{\rho}$ = 4 %) was elastic buckling behavior, and we observed that such a mechanism contributed to an improvement to structural damping as compared to the deformation mechanism at higher relative densities. Moreover, this finding implies that a cellular structure is preferable to a bulk material for the purpose of structural damping. A sample having $\bar{\rho}$ = 4 % exhibited a larger loss tangent than that having $\bar{\rho}$ = 12 % for all V_{soft} values.

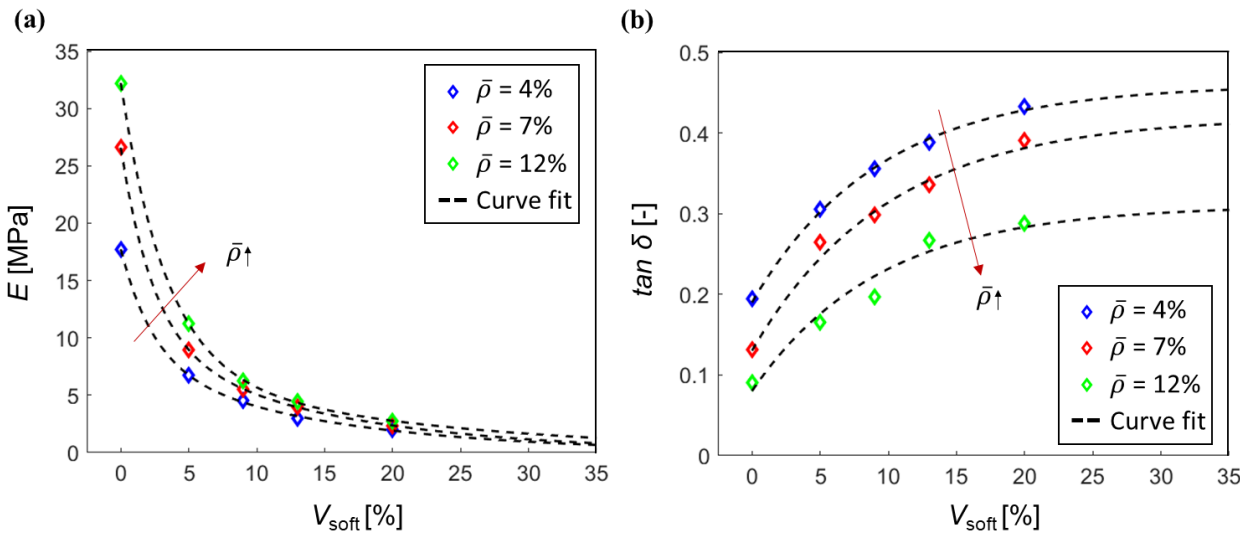

Figure 5.9. Stiffness and damping results from cyclic tests. (a) The effective modulus (E) as a function of V_{soft}. The modulus was inversely proportional to an increase in V_{soft}. (b) Loss tangent (tan δ) as a function of V_{soft}. An increase in V_{soft} led to an improvement in loss tangent.

Table 5.3: Modulus [MPa] of samples.

$\bar{\rho}$ \ V_{soft}	0%	5%	9%	13%	20%
4%	17.725	6.720	4.510	3.012	1.988
7%	26.597	8.969	5.510	4.004	2.337
12%	32.213	11.250	6.250	4.440	2.740

Table 5.4: tan δ of samples.

$\bar{\rho}$ \ V_{soft}	0%	5%	9%	13%	20%
4%	0.194	0.304	0.355	0.389	0.432
7%	0.132	0.264	0.298	0.335	0.391
12%	0.090	0.166	0.197	0.267	0.288

Table 5.5: The coefficients of fitting equations of modulus of samples.

$\bar{\rho}$ \ Coefficients	a	b	c	d	R^2
4%	9.927	-0.4128	7.797	-0.0702	0.9992
7%	16.85	-0.4141	9.747	-0.0709	0.9987
12%	24.8	-0.303	7.42	-0.0503	0.9999

Table 5.6: The coefficients of fitting equations of tan δ of samples.

$\bar{\rho}$ \ Coefficients	a	b	c	R^2
4%	-0.27	-0.1071	0.46	0.9967
7%	-0.29	-0.1006	0.42	0.978
12%	-0.23	-0.1075	0.31	0.9689

To get a better understanding of the structural damping performance of the microlattice, its FOM for the different relative densities was plotted against the volume fraction of soft phase and is shown in Fig. 5.10. It can be seen that the FOM of merit was higher at lower relative densities and decreases with its increase. Like in the case of intrinsic damping, a peak FOM is seen at a certain volume fraction of soft phase, after which it gradually decreases. The samples with $\bar{\rho}$ of 4% and 7% showed a peak FOM at around 5% V_{soft}, whereas samples with $\bar{\rho}$ of 4% showed a peak at around 10% V_{soft}. This is because the loss tangent at high relative densities reaches its asymptotic value much earlier than that at lower relative densities. Since the structural damping has a contribution from intrinsic damping, the peak in FOM is seen at similar soft phase volume fractions in either case.

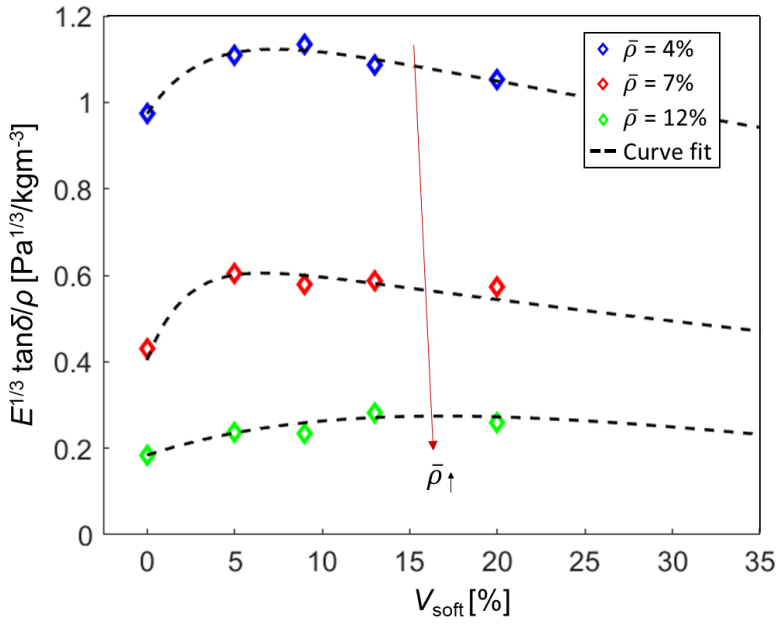

Figure 5.10. The figure of merit as a function of V_{soft}. FOM can be tuned to have a peak when V_{soft} is approximately 10%.

Again, in order to represent the FOM obtained from structural damping over a range of values of relative density of unit cell, $\bar{\rho}$, and volume fraction of soft phase, V_{soft}, a 2D map, as shown in figure 5.11, is presented. The map is generated using curve fits obtained from figures 5.9(a) and 5.9(b). As in the case of intrinsic damping, the FOM is maximum at low relative densities as elastic buckling is a major contributor to the structural energy dissipation mechanism. As the relative density increases, the damping and FOM decreases. This implies that cellular topology with low relative densities provides better performance in terms of FOM when compared to bulk materials. However, this map does not show the FOM for relative densities above 12% as it is hard to predict the energy dissipation mechanism in this regime. This study is only concerned with low-density regimes.

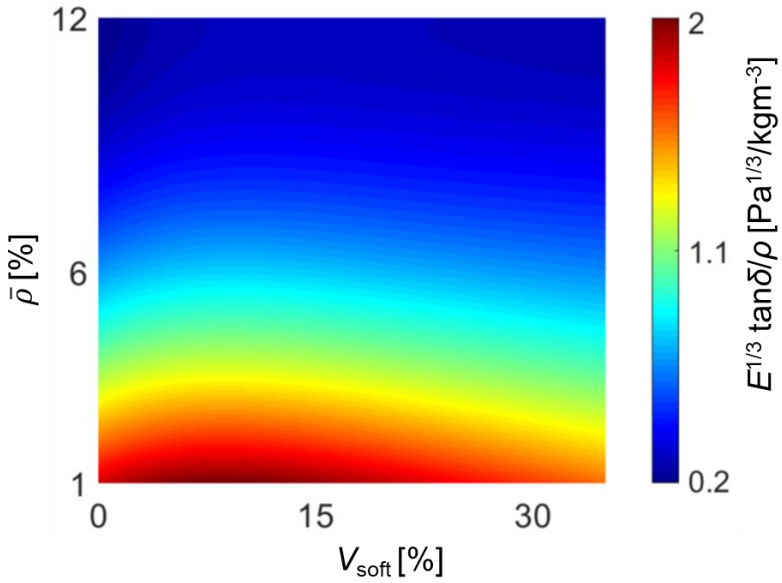

Figure 5.11. Tunability maps for structural damping performance in terms of the figure of merit obtained from experimental measurements.

5.6. Quantitative assessment of CFRP microlattice design

In order to quantitatively assess the performance of the designed CFRP microlattice in comparison to other families of materials and commercially available CFRP, an Ashby chart is presented in

Fig. 5.12. The figure was generated using the CES EduPack 2018 software package developed by Granta Design. The stiffness-to-weight ratio ($E^{1/3}/\rho$) was plotted against the mechanical loss coefficient (tan δ). The dotted lines on the plot represent the design selection lines for the chosen FOM. All materials lying along a line have the same value of FOM, $E^{1/3}\tan\delta/\rho$. Its value increases as we move towards the top-right corner of the plot. The values of FOM, measured from the static and dynamic test for different relative densities and soft phase volume fractions, are bundled together to represent the overall damping performance of the design and is highlighted in orange on the map. It was observed that the microlattice FOM improved by almost two orders of magnitude when compared to commercially available CFRP. Looking at the stiffness-to-weight ratio and mechanical loss coefficient individually, the microlattice exhibits $E^{1/3}/\rho$ close to that of ceramics and commercial CFRP. Simultaneously, the design also exhibits large values of tan δ, comparable to that of elastomers. This design gives us the capability to mimic the performance of natural materials while being able to make use of the other advantages of carbon fiber composites. Also, the properties can be tuned according to the application and FOM required.

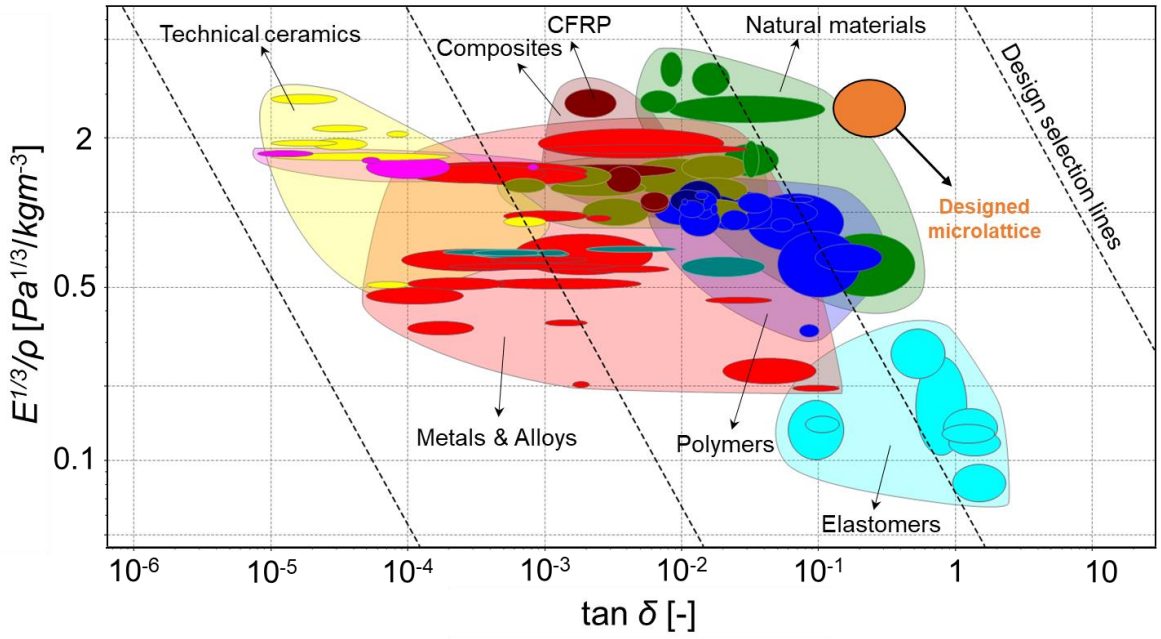

Figure 5.12. Assessment of the lightweight cellular CFRP microlattice developed in this work. The orange ellipse represents the envelope of experimental results for an overall damping property.

Chapter 6: Applications, Conclusions and Future work

6.1. Applications

The presented work can find applications in fields where lightweight structural materials with good vibration damping properties are required. The results from this study can be applied to any lattice design or even to bulk materials. The relative density and soft phase volume fraction can be tuned according to the stiffness and damping combination required. It can also be tuned based on the temperature and frequency range. This flexibility in the choice of material properties allows for a wider range of applications in which this study can be used.

One such application would be aerospace panels. Vibrations damping in aircraft and spacecraft leads to large energy losses. Sound is one of the major source of energy loss in them. Vibrations phenomena like flutter and buffet in structural panels could result in catastrophic disasters. Also, excessive vibrations reduce the efficiency of the system, making air and space travel expensive. As a result, there is a need for effective vibration control in these structures. Previously, several techniques of vibration control have been studied. Fuller et al. [39] and Maury et al. [40] studied the damping of vibrations through active control. However, these techniques require expensive hardware and are usually less effective when compared to passive vibration control. Hence, as an alternative, a design presented in this study can be used. As shown in Fig. 6.1, the panels can be a cellular Reuss structure. This makes it light, stiff and provides high damping, making it ideal for such applications. This theory could also be extended to other applications like automotive panels, sporting equipment, naval structures, wheels.

6.2. Conclusions

In this work, a scalable tape-casting-integrated multi-material stereolithography process capable of fabricating dissipative soft inclusions embedded in a viscous, highly loaded carbon fiber reinforced resin is presented. The process was achieved by recoating the highly viscous resin with an uniformly thin film via the doctor blade and by multiple vats allowing two or more material selection. This process is not limited to the fabrication of CFRP composites but can also be applied to other types of viscous resins. The mechanical properties of CFRP composites fabricated using this system were tested. The results show improvement in properties when compared to other literature. However, the properties are closer to the lower theoretical bound, indicating at a scope for improvement.

Using the multi-material system, a lightweight cellular CFRP microlattice having the Reuss layout was designed, fabricated and investigated analytically and experimentally. Through DMA tests and quasi-static cyclic compression tests at small and large strains respectively, it was observed that small volume fraction of the soft phase was adequate to improve both intrinsic and structural damping performance with some compensation in the effective stiffness. Tunability maps for the intrinsic and structural damping were also developed by using the experimental measurements for design usefulness in terms of FOM ($E^{1/3}\tan\delta/\rho$). The present microlattice was compared with the universe of existing materials, indicating that our microlattice exhibited a comparable stiffness per density as commercial CFRPs and technical ceramics and composites and high damping as elastomers. Finally, the applications of this design are presented.

6.3. Future work

The parts fabricated and tested in this study are few millimeters in length. For real-world applications, larger parts need to be fabricated and tested. In order to achieve this, the current 3D printing system has to be enhanced to print large scale samples. A system was set up to attempt this and the CFRP sample printed is shown in Fig. 6.2. However, the printed sample suffered from large suction forces due to the high viscosity of the resin and large print areas. Another challenge to large scale printing is that the fiber alignment's effects on the mechanical properties become more prominent. Hence at larger scales, it is important to relate the fiber alignment with the mechanical properties. It would also be beneficial to have a system capable of out-of-plane alignment.

Also, the sample shown in the figure was of a single material. Further studies are needed to reduce the suction forces and print high-quality parts. Also, the setup needs to be redesigned and re-coded to allow multi-material printing.

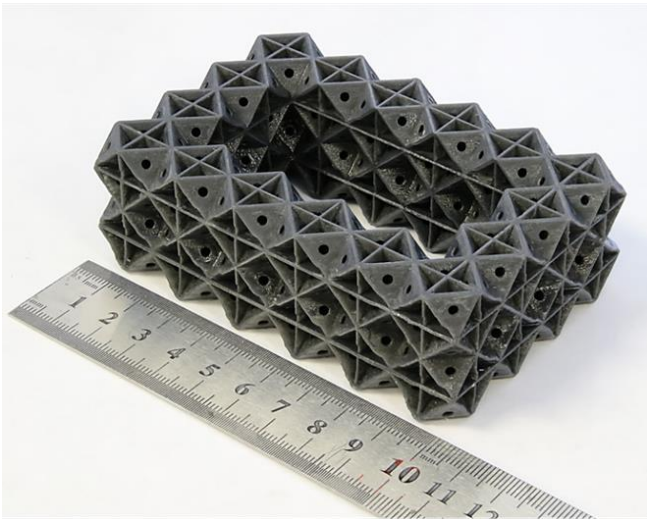

Figure 6.1. Snapshot of large-scale CFRP sample printed.

Another scope for future work is related to the mechanical properties of CFRP composites. As was seen in Fig. 3.7 in section 3.5, the measured values for stiffness are close to the lower bound and there is a lot of scope to increase the stiffness of the composite. One such prospective is the better

alignment of the fibers. Although the tape-casting method helps in the alignment, it is not very effective at higher CF loadings. Other ways to improve the alignment can be studied. Computational methods to predict the alignment of fibers exist. These methods can be applied to the CFRP resin to determine the relationship between fiber alignment and mechanical properties. Also, the stiffness of CFRP increases with increase in length of the carbon fibers. The mechanical properties with longer fiber lengths can be tested to determine its scaling.

6.4. Research contributions

The efforts of several individuals went into this study. The contribution of each is summarized below-

1. Ruthvik Kadam (author) –
    - Literature review and thesis definition.
    - AM system process parameter optimization experiments.
    - Analytical and experimental studies of two-phase viscoelastic composites.
    - Design, fabrication and experimental testing of high stiffness and high damping CFRP microlattice.
    - Analysis of experimental data.
    - Generation of Ashby charts.
2. Zhenpeng Xu –
    - CAD modeling and setup of AM system.
    - AM system process parameter optimization experiments.
    - Design of high stiffness and high damping CFRP microlattice.
    - Analysis of experimental data.
3. Chansoo Ha –
    - Review of work and suggestions in all stages.

References

[1] M. F. Ashby, "Designing Hybrid Materials," in *Materials Selection in Mechanical Design*, Elsevier Ltd. , 2011, p. 308.

[2] X. Zheng et al., "Ultralight, ultrastiff mechanical metamaterials," *Science,* vol. 344, no. 6190, pp. 1373-1377, 2014.

[3] N. A. Fleck, V. S. Deshpande and M. F. Ashby, "Micro-architectured materials: past, present and future," *Proc. of the Royal Soc. A,* vol. 466, no. 2495, 2010.

[4] E. Graesser and C. Wong, "The Relationship of Traditional Damping Measures for Materials with High Damping Capacity: A Review," 2019.

[5] R. Lakes, "Dynamic Behaviour," in *Viscoelastic Materials*, Cambridge University Press, 2009, pp. 55-66.

[6] J. D. Irwin, Basic Engineering Circuit Analysis, New York: Macmillan, 1989.

[7] F. Ning, W. Cong, J. Qiu, J. Wei and S. Wang, "Additive manufacturing of carbon fiber reinforced thermoplastic composites using fused deposition modeling," *Composites Part B: Engineering,* vol. 80, pp. 369-378, 2015.

[8] F. Ning, W. Cong, J. Wei, S. Wang and M. Zhang, "Additive Manufacturing of CFRP Composites Using Fused Deposition Modeling: Effects of Carbon Fiber Content and Length," in *ASME 2015 International Manufacturing Science and Engineering Conference*, Charlotte, NC, 2015.

[9] H. L. Tekinalp, V. Kunc, G. M. Velez-Garcia, C. E. Duty, L. J. Love, A. K. Naskar, C. A. Blue and S. Ozcan, "Highly oriented carbon fiber–polymer composites via additive manufacturing," *Composites Science and Technology,* vol. 105, pp. 144-150, 2014.

[10] X. Zheng, W. Smith, J. Jackson, B. Moran, H. Cui, D. Chen, J. Ye, N. Fang, N. Rodriguez, T. Weisgraber and C. M. Spadaccini, "Multiscale metallic metamaterials," *Nature Materials,* vol. 15, pp. 1100-1106, 2016.

[11] H. Cui, R. Hensleigh, H. Chen and X. Zheng, "Additive Manufacturing and size-dependent mechanical properties of three-dimensional microarchitected, high-temperature ceramic metamaterials," *J. of Mat. Research,* vol. 33, no. 3, pp. 360-371, 2018.

[12] R. M. Hensleigh, H. Cui, J. S. Oakdale, J. C. Ye, P. G. Campbell, E. B. Duoss, C. M. Spadaccini, X. Zheng and M. A. Worsley, "Additive manufacturing of complex micro-architected graphene aerogels," *Materials Horizons,* vol. 5, pp. 1035-1041, 2018.

[13] M. F. Ashby, A. G. Evans, N. A. Fleck and L. J. Gibson, "Metal Foams: A Design Guide," *Butterworth Heinemann, Oxford, UK,* 2000.

[14] L. J. Gibson and M. F. Ashby, Cellular Solids: Structures and Properties, Cambridge, UK: Cambridge University Press, 1999.

[15] H. N. G. Wadley, N. A. Fleck and A. G. Evans, "Fabrication and structural performance of periodic cellular metal sandwich structures," *Composites Science and Technology,* vol. 63, no. 16, pp. 2331-2343, 2003.

[16] L. Vladevit, J. W. Hutchinson and A. G. Evans, "Structurally optimized sandwich panels with prismatic cores," *Int. J. Solid Struct.,* 2004.

[17] J. W. Hutchinson and N. Wicks, "Optimal truss plates," *Int. J. Solids Struct.,* 2001.

[18] L. Valdevit, Z. Wei, C. Mercer, F. W. Zok and A. G. Evans, "Structural performance of near-optimal sandwich panels with corrugated cores," *Int. J. Solids Struct.,* 2006.

[19] A. G. Evans, M. Y. He, V. S. Deshpande, J. W. Hutchinson, A. J. Jacobsen and W. B. Carter, "Concepts for enhanced energy absorption using hollow micro-lattices," *Int. J. Impact Eng.,* 2010.

[20] H. J. Rathbun et al., "Performance of metallic honeycomb-core sandwich beams under shock loading," *Int. J. Solids Struct.,* 2006.

[21] T. A. Schaedler et al., "Designing metallic microlattices for energy absorber applications," *Adv. Eng. Mater.,* vol. 16, no. 3, p. 276–283, 2014.

[22] G. M. Sessler and J. Hillenbrand, "Electromechanical response of cellular electret films," *Appl. Phys. Lett.,* vol. 75, no. 21, pp. 3405-3407, 1999.

[23] J. Banhart, J. Baumeister and M. Weber, "Damping properties of aluminium foams," *Mater. Sci. Eng,* 1996.

[24] T. Pritz, "Dynamic young's modulus and loss factor of plastic foams for impact sound isolation," *J. Sound Vib.,* 1994.

[25] A. Asadpoure, M. Tootkaboni and L. Valdevit, "Topology optimization of multiphase architected materials for energy dissipation," *Comput. Methods Appl. Mech. Eng.,* vol. 325, pp. 314-329, 2017.

[26] S. Shan et al., "Multistable Architected Materials for Trapping Elastic Strain Energy," *Adv. Mater.,* vol. 27, no. 29, pp. 4296-4301, 2015.

[27] B. Haghpanah, L. Salari-Sharif, P. Pourrajab, J. Hopkins and L. Valdevit, "Architected Materials: Multistable Shape-Reconfigurable Architected Materials (Adv. Mater. 36/2016)," *Adv. Mater.,* vol. 28, no. 36, p. 8065, 2016.

[28] C. Sun, N. Fang, D. M. Wu and X. Zhang, "Projection micro-stereolithography using digital micro-mirror dynamic mask," *Sensors and Actuators A: Physical,* vol. 121, no. 1, pp. 113-120, 2005.

[29] X. Song, Y. Chen, T. W. Lee, S. Wu and L. Cheng, "Ceramic fabrication using Mask-Image-Projection-based Stereolithography integrated with tape-casting," *J. Manuf. Processes,* vol. 20, pp. 456-464, 2015.

[30] X. Zheng et al., "Design and optimization of a light-emitting diode projection micro-stereolithography three-dimensional manufacturing system," *Rev. Sci. Instrum.,* vol. 83, no. 12, 2012.

[31] G. D. Goh, Y. L. Yap, S. Agarwala and W. Y. Yeong, "Recent Progress in Additive Manufacturing of Fiber Reinforced Polymer Composite," *Advanced Materials Technologies,* vol. 4, no. 1, pp. 1-22, 2019.

[32] F. Ning, W. Cong, J. Qiu and S. Wang, "Additive manufacturing of carbon fiber reinforced thermoplastic composites using fused deposition modeling," *Composites Part B: Engineering,* vol. 80, pp. 369-378, 2015.

[33] C. P. Chen and R. S. Lakes, "Analysis of high-loss viscoelastic composites," *J. of Mat. Sci.,* vol. 28, no. 16, pp. 4299-4304, 1993.

[34] L. Salari-Sharif, L. Valdevit and T. A. Schaedler, "Energy dissipation mechanisms in hollow metallic microlattices," *J. Mater. Res.,* vol. 29, no. 16, pp. 1755-1770, 2014.

[35] R. Lakes, "Viscoelastic Composite Materials," in *Viscoelastic Materials*, Cambridge University Press, 2009, pp. 344-365.

[36] J. B. Berger, H. G. N. Wadley and R. M. McMeeking, "Mechanical metamaterials at the theoretical limit of isotropic elastic stiffness," *Nature,* pp. 533-537, 2017.

[37] V. S. Deshpande, N. A. Fleck and M. F. Ashby, "Effective properties of the octet-truss lattice material," *J. Mech. Phys. Solids,* 2001.

[38] L. Dong, V. Deshpande and H. Wadley, "Mechanical response of Ti-6Al-4V octet-truss lattice structures," *Int. J. Solids Struct.,* 2015.

[39] C. R. Fuller, S. D. Snyder, C. H. Hansen and R. J. Silcox, "Active Control of Interior Noise in Model Aircraft Fuselages," *AIAA,* vol. 30, no. 11, 1992.

[40] C. Maury, P. Gardonio and S. J. Elliott, "Active Control of the Flow-Induced Noise," *AIAA,* vol. 39, no. 10, 2001.